

## Article

# New Low-Dimensional Organic–Inorganic Lead Halide Hybrid Systems Directed by Imidazo[1,5-*a*]pyridinium-Based Cation or Imines: Synthesis, Structures, Non-Covalent Interactions and Optical Properties

Olga Yu. Vassilyeva <sup>1,\*</sup>, Elena A. Buvaylo <sup>1</sup>, Oksana V. Nesterova <sup>2</sup>, Alexandre N. Sobolev <sup>3</sup>  
and Dmytro S. Nesterov <sup>2,\*</sup>

<sup>1</sup> Department of Chemistry, Taras Shevchenko National University of Kyiv, 64/13 Volodymyrska Str., 01601 Kyiv, Ukraine

<sup>2</sup> Centro de Química Estrutural, Institute of Molecular Sciences, Instituto Superior Técnico, Universidade de Lisboa, Av. Rovisco Pais, 1049-001 Lisboa, Portugal

<sup>3</sup> School of Molecular Sciences, M310, University of Western Australia, Perth, WA 6009, Australia

\* Correspondence: vassilyeva@univ.kiev.ua (O.Y.V.); dmytro.nesterov@tecnico.ulisboa.pt (D.S.N.)

**Abstract:** The organic–inorganic lead halide hybrids comprising semiconducting perovskite components and organic modules have proven to be promising candidates for optoelectronic applications. The modulation of the inorganic components as optical centres by diverse organic cationic templates is under intense investigation. Herein, we successfully prepared new one-dimensional lead halide hybrid perovskites  $[L1]_{2n}[Pb_2Cl_6]_{n\infty} \cdot nH_2O$  (**1**) and  $[PbBr_2(L2)]_{n\infty} \cdot 0.5nH_2O$  (**2**), and the dimeric complex  $[PbBr_2(L3)]_2$  (**3**) in water media. In **1**, 2-(2-hydroxyethyl)-2H-imidazo[1,5-*a*]pyridinium cation  $[L1]^+$  resulted from the oxidative condensation–cyclization between formaldehyde, ethanolamine and 2-pyridinecarbaldehyde (2-PCA); the polydentate Schiff base ligands L2 and L3 formed in the in situ condensation of 2-PCA and ethanolamine or ethylenediamine, respectively. The lead chloride hybrid **1** contains the previously unreported type of a  $[Pb_2Cl_6]_{\infty}$  double chain constructed from three-edge- and five-edge-sharing  $PbCl_6$  octahedra, and cations forming  $\pi$ -bonded stacks aligned along the inorganic wires. In the crystal of **2**, pairs of the double-side organically decorated  $[PbBr_2(L2)]_{\infty}$  chains built of corner-sharing  $PbBr_3N_2O$  octahedra arrange hydrophilic channels to host water molecules. In the solid state, the identically stacked dimers of **3** form columns parallel to the *ab* plane with the  $Pb_2Br_4$  moieties in the column being strictly coplanar. Hirshfeld surface analysis was used to rationalize the packing patterns through hydrogen bonds of O–H...O/Cl and C–H...O/Cl types with the involvement of OH groups of  $[L1]^+$ , L2 and water molecules in **1** and **2**, as well as C–H...Br hydrogen bonding in **2** and **3**. The QTAIM analysis of non-covalent interactions in **1–3** was performed. According to the analysis of the solid-state UV–visible reflectance spectra by a Tauc plot, the optical band gap values of **1**, **2** and **3** as direct gap semiconductors were estimated to be 3.36, 3.13 and 2.96 eV, respectively.

**Keywords:** crystal structure; organic–inorganic hybrid; lead(II) perovskite; Schiff-base ligand; Hirshfeld surface analysis; QTAIM analysis; DFT calculations; reflectance spectra; band gap



**Citation:** Vassilyeva, O.Y.; Buvaylo, E.A.; Nesterova, O.V.; Sobolev, A.N.; Nesterov, D.S. New Low-Dimensional Organic–Inorganic Lead Halide Hybrid Systems Directed by Imidazo[1,5-*a*]pyridinium-Based Cation or Imines: Synthesis, Structures, Non-Covalent Interactions and Optical Properties. *Crystals* **2023**, *13*, 307. <https://doi.org/10.3390/cryst13020307>

Academic Editors: Helmut Cölfen and Leonid Kustov

Received: 28 January 2023

Revised: 6 February 2023

Accepted: 10 February 2023

Published: 13 February 2023



**Copyright:** © 2023 by the authors. Licensee MDPI, Basel, Switzerland. This article is an open access article distributed under the terms and conditions of the Creative Commons Attribution (CC BY) license (<https://creativecommons.org/licenses/by/4.0/>).

## 1. Introduction

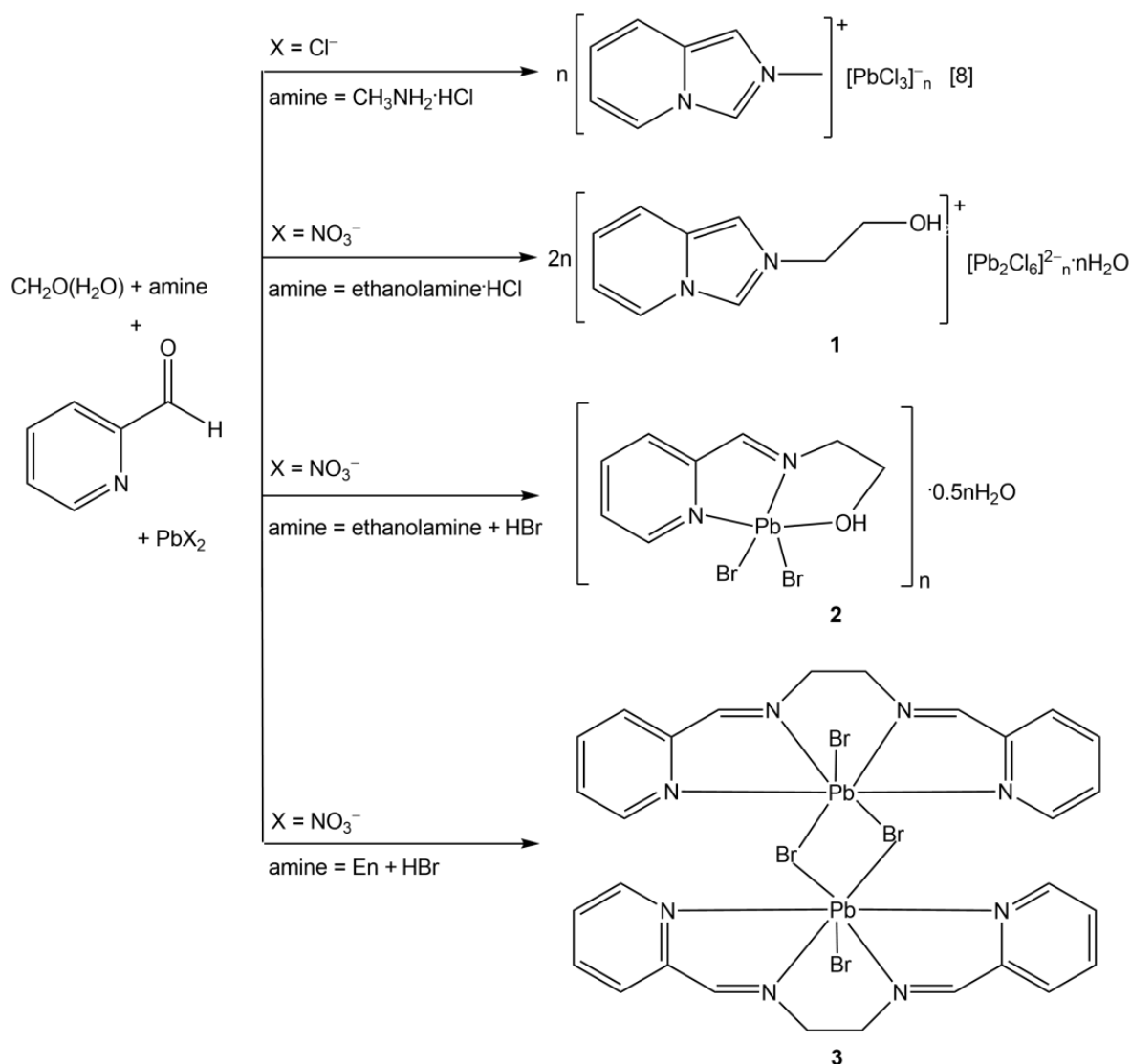
The versatile optoelectronic properties of organic–inorganic hybrid metal halides make them an attractive alternative to photovoltaic devices utilizing a conventional crystalline silicon solar cell or emerging dye-sensitized solar cells, organic tandem cells and quantum dot cells [1]. In addition, due to their structural richness, semiconducting, electrical and optical properties, as well as processability in solution using low temperature techniques, perovskite-based hybrids are promising materials for use in other optoelectronic devices

such as light-emitting diodes (LEDs), photodetectors, semiconductor optical amplifiers and lasers [2,3].

Considering the solid-state arrangement, lead halide hybrid perovskites are built of  $\text{PbHal}_6$  octahedra that share corners, edges or faces to form structures with dimensionality varying from zero (0D) to three (3D), templated by organic cations. The dimensionality and geometry of the inorganic framework determine the optical and electrical properties of the material, while the organic cation can alter/tune its optoelectronic characteristics by modifying this framework. The broadband emission of lead halide hybrid perovskites was proposed to originate from the intrinsic excited electron–hole pairs bound to a deformable lattice (self-trapped excitons), rather than from emissive extrinsic dopants or surface defect sites [4]. There is growing evidence that 1D systems—which often combine several modes of connectivity within a single lead(II) halide chain, depending on the number of bridging halides—create the strong quantum confinement to enable easier exciton self-trapping [5,6].

Recently, we proposed an advantageous synthetic procedure for preparing organic–inorganic hybrid halometalate salts with substituted imidazo[1,5-*a*]pyridinium cations [7–12]. Imidazo[1,5-*a*]pyridines are fused nitrogen-containing bicyclic systems of interest in many research areas, e.g., material science and pharmaceuticals [13,14]. They also demonstrate enhanced fluorescence intensity combined with high quantum yield [15,16]. The organic cation formation occurs in the interaction of equimolar amounts of two aldehydes—formaldehyde (FA) and 2-pyridinecarbaldehyde (2-PCA)—with amine in aqueous media [8,11,12]. The oxidative cyclocondensation is catalyzed by acid that is conveniently introduced as the amine adduct; the cation prepared in situ does not require isolation. The reaction of the preformed heterocyclic cation synthesized using methylamine hydrochloride and metal halides yielded hybrid compounds  $[\text{L}]_n[\text{PbCl}_3]_{n\infty}$ ,  $[\text{L}]_2[\text{ZnCl}_4]$  [8] and  $[\text{L}]_2[\text{CdCl}_4]$  [11], as well as mixed-halide analogues of the latter [12], where  $\text{L}^+$  is 2-methyl-imidazo[1,5-*a*]pyridinium cation. The photophysical properties of the organic–inorganic 1D perovskite  $[\text{L}]_n[\text{PbCl}_3]_{n\infty}$  and 0D pseudo-layered hybrid  $[\text{L}]_2[\text{ZnCl}_4]$  were presumed to originate from the synergistic effects of the electronic structure of the cation and the solid-state architectures.

In the present work, the developed approach was extended to replace  $\text{CH}_3\text{NH}_2\cdot\text{HCl}$  with ethanolamine (Ea) hydrochloride, as summarized in Scheme 1, to obtain lead halide hybrid compounds with another electron-deficient cation, 2-(2-hydroxyethyl)-2H-imidazo[1,5-*a*]pyridinium  $[\text{L1}]^+$ . Given that hydrogen bonds may impact important properties of the material due to their directionality and collective strength, Ea was chosen to examine the effect of introducing hydroxyl (–OH) functionality in the cation onto the resulting hybrid structure. The  $[\text{L1}]^+$  cation templated the formation of a 1D chloroplumbate(II) wire in  $[\text{L1}]_{2n}[\text{Pb}_2\text{Cl}_6]_{n\infty}\cdot n\text{H}_2\text{O}$  (**1**), the hybrid perovskite structure of which was confirmed by X-ray crystal structure analysis. Further replacement of chloride with bromide anion was realized by the addition of the necessary acid component, HBr, directly to the reaction media. For comparison reasons, the study was supplemented with an analogous synthesis involving the ‘ $\text{NH}_2$ ’ alternative of Ea, ethylenediamine (En), to probe hydrogen bonding with amino group. In contrast, the isolated Pb(II) bromides appeared to bear Schiff-base ligands *N*-(2-pyridylmethylene)ethanolamine, L2, and *N,N'*-bis(2-pyridylmethylene)ethylenediamine, L3, produced in the amine-aldehyde condensation reactions between 2-PCA and Ea or En, respectively. Herein, we report the preparation, crystal structures, spectroscopic characterization and optical study of the new 1D hybrid lead halide perovskites  $[\text{L1}]_{2n}[\text{Pb}_2\text{Cl}_6]_{n\infty}\cdot n\text{H}_2\text{O}$  (**1**) and  $[\text{PbBr}_2(\text{L2})]_{n\infty}\cdot 0.5n\text{H}_2\text{O}$  (**2**), and the dimeric Schiff-base complex  $[\text{PbBr}_2(\text{L3})]_2$  (**3**). The Hirshfeld surface (HS) analysis was used to examine the packing patterns through non-covalent interactions. The quantum theory of atoms in molecules (QTAIM) was employed to perform the topological analysis of the electron density.



**Scheme 1.** Reaction schemes and structural formulas of  $[\text{L}]_n[\text{PbCl}_3]_{n\infty}$  [8],  $[\text{L}1]_{2n}[\text{Pb}_2\text{Cl}_6]_{n\infty} \cdot n\text{H}_2\text{O}$  (1),  $[\text{PbBr}_2(\text{L}2)]_{n\infty} \cdot 0.5n\text{H}_2\text{O}$  (2) and  $[\text{PbBr}_2(\text{L}3)]_2$  (3).

## 2. Experimental Section

### 2.1. Materials and General Methods

For the synthesis of lead compounds, 2-PCA (Merck) was used as received; all other chemicals were purchased from local suppliers and used without further purification. All solvents were of AP-grade; all the experiments were carried out in air. Elemental analyses for C, H and N were performed with a Perkin–Elmer 2400 analyzer. The  $^1\text{H}$  NMR spectra of 1–3 in  $\text{DMSO-}d_6$  were measured using a Mercury 400 Varian spectrometer at 400 MHz at r.t. The chemical shifts ( $\delta$ ) values are given in ppm downfield from internal  $\text{Me}_4\text{Si}$ .  $J$  values are in hertz. The FT–IR spectra were recorded on a PerkinElmer 1600 FT–IR instrument from KBr pellets in the  $400\text{--}4000\text{ cm}^{-1}$  region. Optical diffuse reflectance measurements were performed using a Shimadzu UV-2600i spectrophotometer equipped with the 60 mm integrating sphere operating in the  $220\text{--}1400\text{ nm}$  region. Ground powder samples were placed in a powder sample holder;  $\text{BaSO}_4$  was used as the reference of 100% reflectance. The reflectance data were converted to absorption according to Kubelka–Munk function  $\alpha/S = (1 - R)^2 (2R)^{-1}$ , where  $R$  represents the reflectance and  $\alpha$  and  $S$  are the absorption and scattering coefficients, respectively, from which the band gap values were estimated by a Tauc plot [17,18]. HS and fingerprint plots were generated by *CrystalExplorer* 21.5 program (revision 608bb32) [19].

### 2.1.1. Synthesis of $[L1]_{2n}[Pb_2Cl_6]_{n\infty} \cdot nH_2O$ (**1**)

FA solution was prepared by dissolving paraform (0.13 g, 4.5 mmol) in 10 mL boiling deionized water in a 50 mL conic flask. After cooling at r.t., solid Ea·HCl (0.39 g, 4 mmol) was introduced into the FA solution, which was stirred vigorously at r.t. for half an hour. Then, the pale-yellow solution was filtered and left open overnight. The next day, 2-PCA (0.38 mL, 4 mmol) was added and the solution was kept stirring for 1 h while getting brownish. A subsequent dropwise addition of  $Pb(NO_3)_2$  (0.33 g, 1 mmol) dissolved in DMF (5 mL) induced the precipitation of a small amount of a yellow residue. The mixture was kept stirring for another hour, then filtered and the brown solution was allowed to stand at r.t. Colourless needles of **1** suitable for X-ray crystallography were formed within a few days after addition of  $iPrOH$  (2 mL). The crystals were filtered off, washed with  $iPrOH$  and finally dried in air. Yield based on  $Pb(NO_3)_2$ : 47%. FT-IR ( $\nu$ ,  $cm^{-1}$ ): 3400vs, 3116s, 3072, 3060, 2954, 2928, 2880, 1654, 1560, 1544, 1508, 1448, 1384, 1350, 1328, 1258, 1224, 1150s, 1132, 1076, 946, 922, 880, 796s, 750, 666, 636, 428.  $^1H$  NMR (400 MHz, DMSO- $d_6$ ):  $\delta$  (ppm) 10.01 (s, 1H, =N-CH=N-), 8.79 (d,  $J = 7.0$  Hz, py), 8.32 (s, 1H, =C=CH-N-), 7.87 (d,  $J = 9.2$  Hz, 1H, py), 7.26 (dd,  $J = 9.1, 6.7$  Hz, 1H, py), 7.16 (dd,  $J = 9.9, 3.8$  Hz, 1H, py), 5.23 (s, 1H, OH), 4.67 (m, 2H, CH<sub>2</sub>), 3.92 (m, 2H, CH<sub>2</sub>). Analysis calculated for  $C_{18}H_{24}Cl_6N_4O_3Pb_2$  (971.49): C, 22.25; H 2.49; N 5.77%. Found: C 22.39; H 2.28; N 5.52%.

### 2.1.2. Synthesis of $[PbBr_2(L2)]_{n\infty} \cdot 0.5nH_2O$ (**2**)

Compound **2** was synthesized by adopting the procedure similar to that of **1** using Ea (0.24 mL, 4 mmol) and HBr (0.15 mL, 4 mmol) in place of solid Ea·HCl, and dry  $Pb(NO_3)_2$  instead of its solution. Orange prisms of **2** suitable for X-ray crystallography were formed within a week after addition of  $iPrOH$  (3 mL) to the orange solution. Yield based on  $Pb(NO_3)_2$ : 31%. FT-IR ( $\nu$ ,  $cm^{-1}$ ): 3392br, 3180br, 3086, 3062, 3016, 2930, 2900, 2872, 1654, 1590, 1568, 1440, 1314, 1224, 1154, 1108, 1048vs, 1006, 988, 912, 874, 782s, 634, 570, 510, 408.  $^1H$  NMR (400 MHz, DMSO- $d_6$ ):  $\delta$  (ppm) 8.76 (m, 1H, py), 8.50 (s, 1H, -N=CH-py), 8.00 (m, 1H, py), 7.98 (m, 1H, py), 7.62 (m, 1H, py), 4.40 (m, 1H, OH), 3.76 (m, 2H, CH<sub>2</sub>), 3.71 (m, 2H, CH<sub>2</sub>). Analysis calculated for  $C_8H_{11}Br_2N_2O_{1.5}Pb$  (526.20): C, 18.26; H 2.11; N 5.32%. Found: C 18.45; H 2.15; N 5.47%.

### 2.1.3. Synthesis of $[PbBr_2(L3)]_2$ (**3**)

Compound **3** was synthesized by adopting the procedure similar to that of **2** using En (0.26 mL, 4 mmol) in place of Ea. Yellow plate-like crystals of **3** suitable for X-ray crystallography were formed within a week after addition of  $iPrOH$  (3 mL) to the orange solution. Yield based on  $Pb(NO_3)_2$ : 38%. FT-IR ( $\nu$ ,  $cm^{-1}$ ): 3076, 3060, 3008, 2920, 2898, 1662, 1652, 1586s, 1564, 1474, 1434, 1374, 1306s, 1218, 1148, 1104, 1036, 1000s, 986, 942, 782, 748, 626, 506, 406.  $^1H$  NMR (400 MHz, DMSO- $d_6$ ):  $\delta$  (ppm) 8.99 (m, 2H, py), 8.86 (s, 2H, -N=CH-py), 8.01 (m, 4H, py), 7.60 (m, 2H, py), 4.17 (s, 4H, =NCH<sub>2</sub>CH<sub>2</sub>N=). Anal. Calcd for  $C_{14}H_{14}Br_2N_4Pb$  (605.30): C, 27.78; H 2.33; N 9.26%. Found: C 28.04; H 2.45; N 9.38%.

## 2.2. Single Crystal Structure Determination of **1–3**

Crystallographic data for the structures were collected on an Oxford Diffraction Gemini (**1**) and Bruker D8 Quest diffractometers (**2, 3**) using Mo  $K\alpha$  ( $\lambda = 0.71073$  Å) radiation. Following analytical absorption corrections and solution by direct methods, the structures were refined against  $F^2$  with full-matrix least-squares using the program SHELXL-2019/2 [20]. Anisotropic displacement parameters were employed for the non-hydrogen atoms. The (N22, N23A) cation in **1** was modelled as being disordered over two sets of sites with site occupancies constrained to 0.701(5) and its complement. The hydroxyl and water molecule hydrogen atoms (**1, 2**) were located from the experimental data and refined with O–H distances restrained to their idealized values. Other hydrogen atoms were added at calculated positions and refined by the use of a riding model with isotropic displacement parameters based on those of the parent atom. Details of the data collection and processing, structure solution and refinement are summarized in Table 1, while the selected bond lengths and

angles are presented in Table 2. CCDC 2217143, 2223148 and 2223147 contain the supplementary crystallographic data for this paper. These data can be obtained free of charge from the Cambridge Crystallographic Data Centre via [www.ccdc.cam.ac.uk/data-request/cif](http://www.ccdc.cam.ac.uk/data-request/cif).

**Table 1.** Crystallographic parameters and refinement data for 1–3.

Compound	1	2	3
Empirical formula	C <sub>18</sub> H <sub>24</sub> Cl <sub>6</sub> N <sub>4</sub> O <sub>3</sub> Pb <sub>2</sub>	C <sub>16</sub> H <sub>22</sub> Br <sub>4</sub> N <sub>4</sub> O <sub>3</sub> Pb <sub>2</sub>	C <sub>28</sub> H <sub>28</sub> Br <sub>4</sub> N <sub>8</sub> Pb <sub>2</sub>
Formula weight	971.49	1052.39	1210.60
Temperature/K	100(2)	296(2)	296(2)
Crystal system	Triclinic	Orthorhombic	Triclinic
Space group	$P\bar{1}$ (No. 2)	$Pccn$ (No. 56)	$P\bar{1}$ (No. 2)
$a/\text{Å}$	7.5232(3)	9.5345(14)	8.9423(5)
$b/\text{Å}$	11.3164(5)	33.493(5)	9.3263(8)
$c/\text{Å}$	16.5513(6)	7.9626(12)	12.3991(7)
$\alpha/^\circ$	105.748(3)	90	82.812(3)
$\beta/^\circ$	96.367(3)	90	70.156(2)
$\gamma/^\circ$	90.885(3)	90	61.408(2)
$V/\text{Å}^3$	1346.32(10)	2542.7(6)	853.18(10)
Z	2	4	1
Calculated density $D_c/\text{g cm}^{-3}$	2.396	2.749	2.356
Absorption coefficient $\mu/\text{mm}^{-1}$	13.112	19.534	14.569
$F_{000}$	900	1896	556
$\theta$ range for data collection/ $^\circ$	2.547 to 26.372	2.809 to 28.337	2.975 to 29.994
Completeness to $\theta_{\text{max}}$	0.999	0.996	0.997
Reflections collected	11,257	77,380	44,646
Independent reflections	5508 [ $R_{\text{int}} = 0.0330$ ]	3175 [ $R_{\text{int}} = 0.0690$ ]	5257 [ $R_{\text{int}} = 0.0844$ ]
Min. and max. transmission	0.260 and 1.0	0.3359 and 0.7457	0.3640 and 0.7461
Data/restraints/parameters	5508/237/341	3175/3/138	5257/0/190
Reflections ( $I > 2\sigma(I)$ )	4556	2783	4455
GoF	1.000	1.264	1.052
$R1, wR2$ [ $I > 2\sigma(I)$ ]	0.0278, 0.0536	0.0469, 0.1013	0.0446, 0.1158
$R1, wR2$ (all data)	0.0382, 0.0581	0.0547, 0.1044	0.0550, 0.1245
Largest diff. peak and hole/ $e \text{ Å}^{-3}$	1.498 and $-1.159$	1.420 and $-2.146$	2.430 and $-1.690$
CCDC no.	2217143	2223148	2223147

### 2.3. Theoretical Calculations

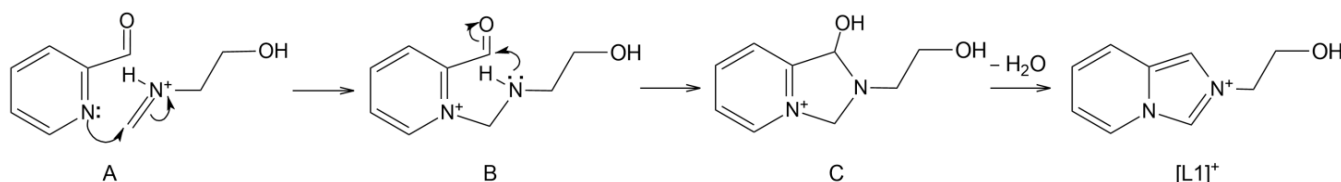
The ORCA 5.0.3 package [21,22] was used for all DFT calculations. Range-separated  $\omega$ B97M-V functional [23] with the ZORA-def2-TZVPP basis sets [24] and SARC/J auxiliary basis set [25,26] were used for all atoms except of Pb, for which the SARC-def2-TZVPP [25] basis set was applied. *AutoAux* keyword [27] was used to generate other auxiliary basis sets in all cases. The zero-order regular approximation (ZORA) [28] was used because of the presence of heavy elements. The crystal field was accounted for by means of the conductor-like polarizable continuum model (C-PCM) [29] with  $\epsilon = \text{infinity}$ . The SCF optimization convergence criteria were settled with *VeryTightSCF* keywords, and integration grids of high density (*Defgrid3* keyword) were employed. Analysis of bond critical points and non-covalent interactions indexes was performed using the Multiwfn 3.8 program [30]. Visualization of the reduced density gradient [31] isosurfaces was performed by means of VMD 1.9.4a53 program [32].

## 3. Results and Discussion

### 3.1. Synthesis and Characterization

The mechanism of the formation of a substituted imidazo[1,5-*a*]pyridinium cation has been suggested by us before [8]. In the present study, the primary addition of Ea·HCl to FA aqueous solution yields 2-(methyleneamino)ethanol (Scheme 2). The subsequent 2-PCA

attack on the protonated Schiff base A initiates condensation with the intermediate B. The intramolecular nucleophilic attack onto the aldehyde carbon atom by the amine nitrogen brings the product of cyclization C, which experiences an irrevocable dehydration reaction affording the aromatic heterocyclic cation [L1]<sup>+</sup>. The dehydration of the five-membered ring results in the formation of two double bonds and the delocalization of the positive charge on N atoms in a resonance structure. The reaction does not require the presence of metal ions.



**Scheme 2.** Proposed mechanism of the formation of [L1]<sup>+</sup> cation.

The lead chloride hybrid perovskite **1** formed by self-assembly from the in situ prepared monovalent organic cations, Pb<sup>2+</sup> and chloride ions at an overall 1PbCl<sub>2</sub>:4CH<sub>2</sub>O:4Ea·HCl:4(2-PCA) mole ratio. It is insoluble in alcohols and water and slightly soluble in *N,N*-dimethylformamide (DMF) and dimethylsulfoxide (DMSO); it is indefinitely stable in air. Similar reaction procedures that used Ea or En combined with HBr did not afford the respective imidazo[1,5-*a*]pyridinium cations, presumably due to the insufficient acid strength.

The IR spectra of **1–3** confirmed the presence of aromatic rings, alkyl and other functional groups (Figures S1–S3). The spectrum of the hybrid compound **1** demonstrates a distinctive pattern, which was suggested to characterize the imidazo[1,5-*a*]pyridinium skeleton [8,11,12]: the sharp very strong peaks attributed to aromatic C–H vibrations (3116–3060 cm<sup>−1</sup>), medium intensity sharp bands at 1654 and 1544 cm<sup>−1</sup> associated with heterocyclic ring stretching, an intense absorption at 1150 cm<sup>−1</sup> and three peaks in the region of out-of-plane C–H bending (796, 750 and 636 cm<sup>−1</sup>). The very intense band, due to ν(O–H) vibration at 3400 cm<sup>−1</sup>, dominated the spectrum; another intense absorption was ascribed to C–O stretching (1076 cm<sup>−1</sup>). In the case of compounds **2** and **3**, the aromatic ν(C–H) bands above 3000 cm<sup>−1</sup> are much weaker. The spectrum of compound **2** is dominated by a peak at 1048 cm<sup>−1</sup> due to ν(C–O), while the absorption of moderate intensity due to O–H stretching (3392 cm<sup>−1</sup>) is broad. ν(C=N) + ν(C=C) stretching frequencies of the metal coordinated Schiff bases are observed at 1654, 1590 cm<sup>−1</sup> (**2**) and 1652, 1586 cm<sup>−1</sup> (**3**).

The compounds are easily distinguishable by their <sup>1</sup>H NMR spectra that demonstrate the sets of signals, as well as the correct alkyl/aromatic proton ratios expected for [L1]<sup>+</sup> cations and the Schiff base ligands. In the room temperature (r.t.) spectrum of compound **1** in DMSO-*d*<sub>6</sub>, CH protons in the imidazolium ring appear as singlets at δ = 10.01 and 8.32 ppm, the alkyl groups protons are observed as multiplets at 4.67 and 3.92 ppm. The imine protons in **2** and **3** are detected at 8.50 and 8.86 ppm, respectively, while the protons of CH<sub>2</sub> groups appear as two multiplets at 3.76 and 3.71 (**2**) and one multiplet at 4.17 ppm (**3**). The hydroxyl protons in **1** and **2** are observed distinctly at 5.23 and 4.40 ppm, respectively.

### 3.2. Structural Description of 1–3

The asymmetric unit of the lead chloride hybrid **1** is comprised of two [L1]<sup>+</sup> cations, [Pb<sub>2</sub>Cl<sub>6</sub>]<sup>2−</sup> anionic fragment and water molecule of crystallization (Figure 1). Two crystallographically non-equivalent cations configurations are very similar; the (N22, N23A) cation is disordered over two sites, with occupancies of 0.701(5) and 0.299(5)−. The pyridinium rings bond distances of their fused heterocyclic cores are uneventful; the N–C bond lengths in the imidazolium entities fall in the range 1.331(7)–1.414(6) Å. The N atoms are planar, showing a sum of three angles of 360°. In the cores, the five- and six-membered rings are nearly coplanar, with the respective dihedral angles of 1.35, 1.73 and 2.98°.

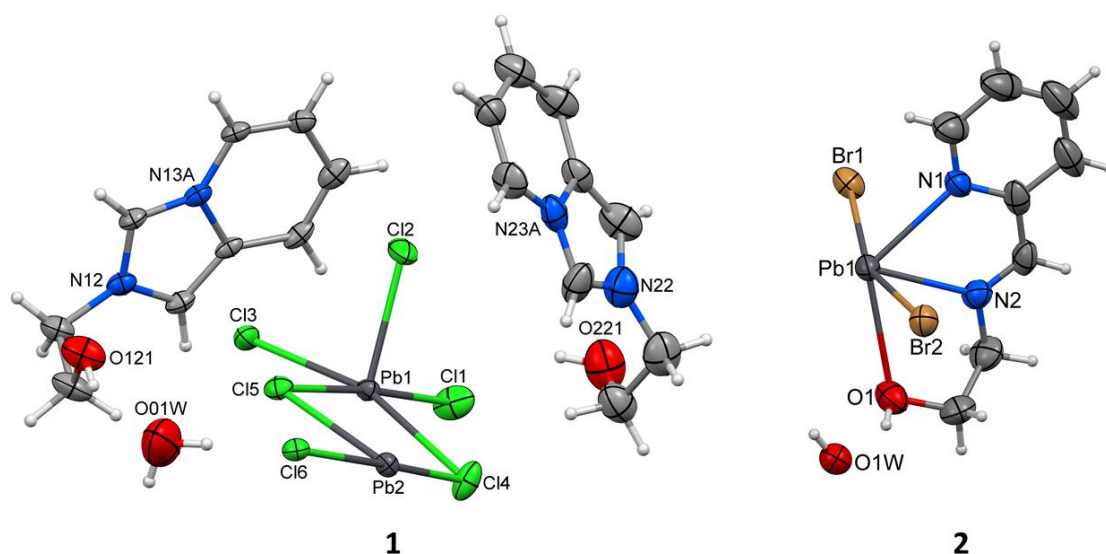


**Figure 1.** Asymmetric units and principal atom labelling for  $[L1]_{2n}[Pb_2Cl_6]_{n\infty} \cdot nH_2O$  (**1**) and  $[PbBr_2(L2)]_{n\infty} \cdot 0.5nH_2O$  (**2**) with the 50% probability ellipsoids. The major component of the disordered (N22, N23A) cation of **1** is shown.

The distorted octahedral environment of Pb1 atom in the anionic motif consists of two terminal, two  $\mu_2$ -Cl and two  $\mu_3$ -Cl atoms, while the distorted octahedron around Pb2 is built of two  $\mu_2$ -Cl and four  $\mu_3$ -Cl ligands (Figure 2a). The metal–chloride distances vary in the range 2.6509(14)–3.1516(14) Å. The average value of 2.907 Å is reasonable for Pb(II) ions in chloroplumbates(II) with strong ionic Pb–Cl bonds [33,34]; the *cis* and *trans* angles at the metal atom fall in the ranges of 77.50(4)–107.33(5)° and 162.86(5)–177.20(4)°, respectively (Table 2), showing a strong degree of distortion of the metal polyhedra. The  $PbCl_6$  octahedra are joined by three-edge- and five-edge-sharing into a 1D twin lead(II) chloride wire of 10.344 Å width, lying in the *a*-axis direction (Figure 2a,b). The bulkier 2-(2-hydroxyethyl)-2H-imidazo[1,5-*a*]pyridinium cation in **1**, if compared to its methyl analogue [8], expectedly templated the formation of a low-dimensional anionic perovskite frame, however, with a different type of a double chain. This set of connectivity modes within a double chain was not observed in the lead(II) chloride hybrid compounds in accordance with our survey of the Cambridge Structural Database [35]. The type of edge-sharing within a double haloplumbate(II) chain shown in the inset of Figure 2b is more frequent and found in, for example, 1D lead chloride perovskites with substituted diammonium and piperidinium dications [6,36].

**Table 2.** Selected bond lengths (Å) and angles (°) in **1–3** [a].

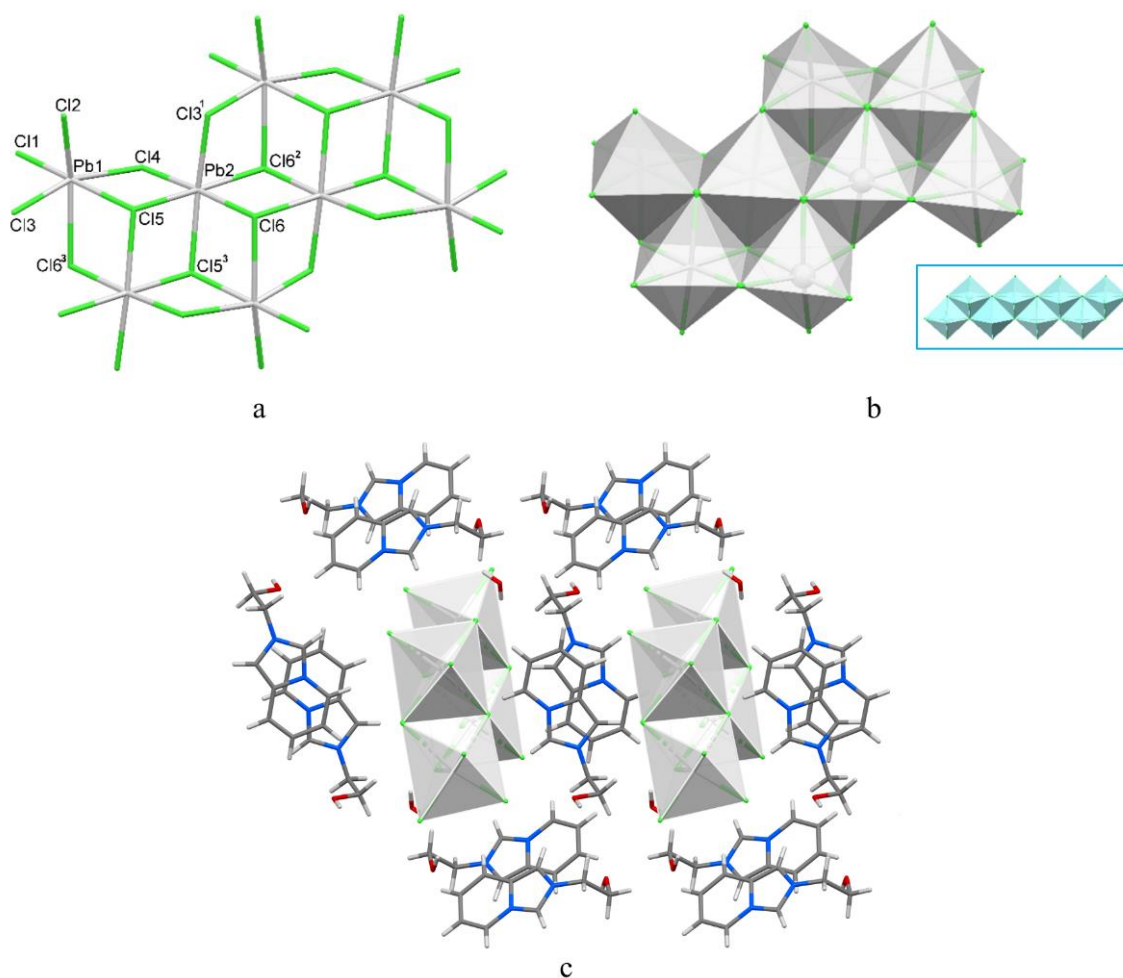
$[L1]_{2n}[Pb_2Cl_6]_{n\infty} \cdot nH_2O$ ( <b>1</b> )			
Pb1–Cl1	2.7587(16)	Pb2–Cl4	2.7924(15)
Pb1–Cl2	2.6509(14)	Pb2–Cl3 <sup>1</sup>	2.8177(14)
Pb1–Cl3	2.8223(13)	Pb2–Cl6 <sup>2</sup>	2.8730(13)
Pb1–Cl4	3.0750(14)	Pb2–Cl5	2.9355(13)
Pb1–Cl5	3.0472(14)	Pb2–Cl6	2.9613(14)
Pb1–Cl6 <sup>3</sup>	3.1516(14)	Pb2–Cl5 <sup>3</sup>	2.9957(14)
Cl2–Pb1–Cl1	93.17(5)	Cl4–Pb2–Cl3 <sup>1</sup>	94.36(5)
Cl2–Pb1–Cl3	86.32(4)	Cl4–Pb2–Cl6 <sup>2</sup>	96.36(4)
Cl1–Pb1–Cl3	94.13(5)	Cl3 <sup>1</sup> –Pb2–Cl6 <sup>3</sup>	82.39(4)
Cl2–Pb1–Cl5	90.30(4)	Cl4–Pb2–Cl5	87.03(4)
Cl1–Pb1–Cl5	175.07(4)	Cl3 <sup>1</sup> –Pb2–Cl5	94.79(4)
Cl3–Pb1–Cl5	89.58(4)	Cl6 <sup>2</sup> –Pb2–Cl5	175.73(3)
Cl2–Pb1–Cl4	107.33(5)	Cl4–Pb2–Cl6	177.20(4)

Table 2. Cont.

Cl1–Pb1–Cl4	95.37(4)	Cl3 <sup>1</sup> –Pb2–Cl6	87.68(4)
Cl3–Pb1–Cl4	162.86(5)	Cl6 <sup>2</sup> –Pb2–Cl6	85.80(4)
Cl5–Pb1–Cl4	80.25(4)	Cl5–Pb2–Cl6	90.89(4)
Cl2–Pb1–Cl6 <sup>3</sup>	161.97(4)	Cl4–Pb2–Cl5 <sup>3</sup>	92.01(5)
Cl1–Pb1–Cl6 <sup>3</sup>	95.85(5)	Cl3 <sup>1</sup> –Pb2–Cl5 <sup>3</sup>	173.17(4)
Cl3–Pb1–Cl6 <sup>3</sup>	77.50(4)	Cl6 <sup>2</sup> –Pb2–Cl5 <sup>3</sup>	99.36(4)
Cl5–Pb1–Cl6 <sup>3</sup>	81.77(4)	Cl5–Pb2–Cl5 <sup>3</sup>	83.07(4)
Cl4–Pb1–Cl6 <sup>3</sup>	87.35(4)	Cl6–Pb2–Cl5 <sup>3</sup>	85.88(4)
<b>[PbBr<sub>2</sub>(L2)]<sub>n∞</sub>·0.5nH<sub>2</sub>O (2)</b>			
Pb1–N1	2.584(7)	Pb1–Br2	2.9777(10)
Pb1–N2	2.562(7)	Pb1–Br1 <sup>4</sup>	3.0764(10)
Pb1–O1	2.839(7)	Pb1–Br1	3.0293(11)
N2–Pb1–N1	64.4(3)	O1–Pb1–Br1 <sup>4</sup>	146.36(15)
N2–Pb1–O1	61.8(2)	Br2–Pb1–Br1 <sup>4</sup>	89.35(3)
N1–Pb1–O1	123.3(2)	N2–Pb1–Br1	84.41(17)
N2–Pb1–Br2	85.72(18)	N1–Pb1–Br1	80.21(16)
N1–Pb1–Br2	80.57(16)	O1–Pb1–Br1	110.23(16)
O1–Pb1–Br2	79.24(16)	Br2–Pb1–Br1	160.70(3)
N2–Pb1–Br1 <sup>4</sup>	149.39(18)	Br1–Pb1–Br1 <sup>4</sup>	90.73(3)
N1–Pb1–Br1 <sup>4</sup>	85.02(18)		
<b>[PbBr<sub>2</sub>(L3)]<sub>2</sub> (3)</b>			
Pb1–N1	2.745(6)	Pb1–Br1	3.0632(9)
Pb1–N2	2.625(5)	Pb1–Br2	2.9599(9)
Pb1–N3	2.621(6)	Pb1–Br1 <sup>3</sup>	3.2525(8)
Pb1–N4	2.808(6)		
N2–Pb1–N1	61.15(17)	N2–Pb1–Br1	84.71(12)
N3–Pb1–N1	123.10(18)	N1–Pb1–Br1	93.02(11)
N3–Pb1–N2	63.60(19)	N4–Pb1–Br1	85.58(12)
N3–Pb1–N4	60.4(2)	Br2–Pb1–Br1	174.31(2)
N2–Pb1–N4	121.93(19)	N3–Pb1–Br1 <sup>3</sup>	149.42(14)
N1–Pb1–N4	176.39(16)	N2–Pb1–Br1 <sup>3</sup>	145.63(13)
N3–Pb1–Br2	81.33(13)	N1–Pb1–Br1 <sup>3</sup>	87.48(13)
N2–Pb1–Br2	89.91(12)	N4–Pb1–Br1 <sup>3</sup>	89.05(15)
N1–Pb1–Br2	85.97(12)	Br2–Pb1–Br1 <sup>3</sup>	102.31(3)
N4–Pb1–Br2	95.75(12)	Br1–Pb1–Br1 <sup>3</sup>	83.22(2)
N3–Pb1–Br1	94.60(13)		

[a] Symmetry codes: <sup>1</sup>  $x - 1, y, z$ ; <sup>2</sup>  $-x, -y + 1, -z + 1$ ; <sup>3</sup>  $-x + 1, -y + 1, -z + 1$ ; <sup>4</sup>  $1/2 - x, y, 1/2 + z$ .

In the crystal, non-equivalent [L1]<sup>+</sup> cations of **1** form separate stacks parallel the *a*-axis with the fused heterocyclic cores of neighboring entities being strictly coplanar (Figure 2c). Centrosymmetrically related trans-oriented [L1]<sup>+</sup> cations are stacked with varying levels of offset, showing the ring centroid distances of 3.456, 3.651 Å for (N12, N13A) and 3.839, 5.258 Å for (N22, N23A) cations enabling the possibility of weak  $\pi$ -bonding [37]. Hydrogen bonds of O–H...O/Cl and C–H...O/Cl types with the involvement of the OH group of the organic cation and water molecule (Table 3) strengthen the hybrid salt structure. The introduction of OH group on the cation enabled a stronger interaction between cationic and anionic counterparts in **1** through additional conventional hydrogen bonding, which is absent in the lead chloride hybrid with methyl derivative of [L1]<sup>+</sup> cation [8]. The new type of a double chain realized in **1** may also be considered a result of such a modification of the organic cation.



**Figure 2.** (a) Fragment of the 1D twin offset chloroplumbate(II) chain in **1**. The symmetry codes have the same numbering as those in Table 2; (b) polyhedral representation of the same fragment; the inset shows a common type of edge-sharing within a double haloplumbate(II) wire; (c) fragment of the crystal packing of **1** demonstrating spatial arrangement of the organic and inorganic counterparts (the major component of the disordered (N22, N23A) cation is shown).

**Table 3.** Geometry of hydrogen bonds for **1–3** (Å and °) <sup>[a]</sup>.

D–H...A	d(D–H)	d(H...A)	d(D...A)	∠(DHA)
<b>[L1]<sub>2n</sub>[Pb<sub>2</sub>Cl<sub>6</sub>]<sub>n∞</sub>·nH<sub>2</sub>O (<b>1</b>) <sup>[b]</sup></b>				
C11–H11...Cl5	0.95	2.90	3.627(5)	134
C12–H12B...Cl2 <sup>1</sup>	0.99	2.96	3.862(6)	152
C13–H13...Cl2 <sup>1</sup>	0.95	2.71	3.558(6)	148
C14–H14...Cl6 <sup>2</sup>	0.95	2.86	3.506(5)	126
C15–H15...Cl6 <sup>2</sup>	0.95	2.86	3.509(5)	127
C17–H17...Cl3 <sup>3</sup>	0.95	2.96	3.529(5)	120
C17–H17...Cl5	0.95	2.88	3.649(5)	139
C22–H22B...Cl1 <sup>3</sup>	0.99	2.81	3.705(11)	150
C23–H23...Cl1 <sup>3</sup>	0.95	2.84	3.481(10)	126
C24–H24...Cl3 <sup>3</sup>	0.95	2.75	3.597(12)	149
C25–H25...O01W <sup>2</sup>	0.95	2.48	3.325(12)	148
C27–H27...Cl2 <sup>4</sup>	0.95	2.85	3.716(14)	153
C221–H22C...O221 <sup>5</sup>	0.99	2.39	3.105(13)	128
C221–H22D...Cl4	0.99	2.80	3.753(12)	161
O01W–H01A...Cl1 <sup>6</sup>	0.85	2.34	3.179(7)	172

Table 3. Cont.

O01W–H01B...C14 <sup>7</sup>	0.85	2.37	3.168(6)	155
O121–H121...O01W	0.84	1.94	2.710(8)	151
O221–H221...C11	0.84	2.24	2.967(8)	145
<b>[PbBr<sub>2</sub>(L2)]<sub>n</sub>∞·0.5nH<sub>2</sub>O (2)</b>				
O1–H1...O1W	0.84(2)	2.06(7)	2.829(10)	152(13)
O1W–H1W...O1 <sup>8</sup>	0.84(2)	1.92(3)	2.740(9)	164(4)
C1–H1A...Br1 <sup>9</sup>	0.93	2.90	3.657(13)	139.3
C2–H2A...Br1 <sup>10</sup>	0.93	2.94	3.845(13)	164.3
C4–H4A...Br1 <sup>11</sup>	0.93	2.90	3.631(11)	136.3
C6–H6A...Br2 <sup>12</sup>	0.93	2.89	3.819(9)	172.8
C8–H8A...Br2 <sup>13</sup>	0.97	3.14	3.881(10)	134.4
<b>[PbBr<sub>2</sub>(L3)]<sub>2</sub> (3)</b>				
C2–H2A...Br1 <sup>14</sup>	0.93	2.88	3.690(8)	147.0
C4–H4B...Br2 <sup>3</sup>	0.93	3.09	3.890(9)	145.2
C6–H6A...Br2 <sup>5</sup>	0.93	3.15	3.977(7)	149.7
C7–H7A...Br2 <sup>5</sup>	0.97	3.16	4.095(8)	161.4
C11–H11A...Br2 <sup>15</sup>	0.93	3.07	3.869(10)	145.1
C13–H13A...Br1 <sup>13</sup>	0.93	2.97	3.684(9)	134.9

[a] Symmetry codes: <sup>1</sup>  $-x + 1, -y, -z + 1$ ; <sup>2</sup>  $-x, -y, -z + 1$ ; <sup>3</sup>  $x - 1, y, z$ ; <sup>4</sup>  $-x + 1, -y, -z$ ; <sup>5</sup>  $-x + 1, -y + 1, -z$ ; <sup>6</sup>  $-x + 1, -y + 1, -z + 1$ ; <sup>7</sup>  $-x, -y + 1, -z + 1$ ; <sup>8</sup>  $-x + 1/2, y, z + 1/2$ ; <sup>9</sup>  $-x + 1/2, y, z + 1/2$ ; <sup>10</sup>  $-x, -y + 1, -z$ ; <sup>11</sup>  $-x - 1/2, y, z + 1/2$ ; <sup>12</sup>  $-x - 1/2, y, z - 1/2$ ; <sup>13</sup>  $x, -y + 3/2, z - 1/2$ ; <sup>14</sup>  $x - 1, y + 1, z$ ; <sup>15</sup>  $x + 1, y - 1, z$ ; <sup>16</sup>  $x + 1, y, z$ . [b] H bonds for the major component of the disordered (N22, N23A) cation are given.

Lead halide hybrid **2**, which crystallizes in the orthorhombic space group *Pccn*, consists of a 1D monobromo-bridged lead(II) polymer and water molecules of crystallization. The asymmetric unit of **2** is shown in Figure 1. In the double-sided, organically decorated chain structure, the nearest six-coordinate environment of each metal atom is formed by one tridentate Schiff base, one terminal and two  $\mu_2$ -Br ligands (Figure 3a,b). The neutral Schiff base ligand chelates the Pb1 ion by the N1 atom of the pyridyl ring, the imine N2 atom and O1 atom of the ethanol group with an average value of the Pb1–N distances of 2.57 Å, and the Pb–O1 bond [2.839(7) Å] being significantly elongated (Table 2). The metal distances to terminal and bridging bromide atoms are similar, with an average of 3.03 Å falling in the usual range for 1D lead(II) bromide systems [38,39]. The additional Pb...Br2{1/2 – x, y, –1/2 + z} contact of 3.378 Å is appreciably larger than the sum of the Shannon ionic radii of the octahedral lead(II) cation and bromide anion [ $r(\text{Pb}^{2+}) + r(\text{Br}^-) = 3.15$  Å] and is barely significant in the construction of the bromoplumbate(II) chain. The bond angles at the Pb1 atom vary from 61.8(2) to 123.3(2)° and from 146.36(15) to 160.70(3)° (Table 2), evidencing the severe distortion of the metal polyhedron. The closest Pb...Pb separation within the chain is 4.4144(6) Å. In the crystal, two bromoplumbate(II) chains related by a crystallographic two-fold axis form a hydrophilic channel to host water molecules held by O–H...O hydrogen bonds (Figure 3c, Table 3). Numerous C–H...Br contacts result in a 3D supramolecular architecture.

Complex **3** belongs to the triclinic space group *P1*; the dimeric molecule is located on an inversion centre (Figure 4). The geometry of Pb1 atom is that of an irregular pentagonal bipyramid, the equatorial plane consisting of four nitrogens from the tetradentate chelate L3 and the centrosymmetrically related bromide ligand Br1{1 – x, 1 – y, 1 – z} of the dimer, with two other bromides—Br1 and Br2—occupying apical positions. The Pb–N bond distances within the range of 2.621(6)–2.804(6) Å (Table 2) agree well with those of two other known Pb(II) complexes with L3 [40,41]. The Pb1–Br1{1 – x, 1 – y, 1 – z} bond is elongated at 3.2525(8) Å, in contrast to the average Pb1–Br1/Br2 bond length of 3.014 Å. The *cis* angles at the lead atom vary from 60.4(2) to 95.75(12)°; the *trans* angles fall in the range 121.93(19)–176.39(16)°. In the dimer, the Pb...Pb' separation is 4.7239(5) Å.

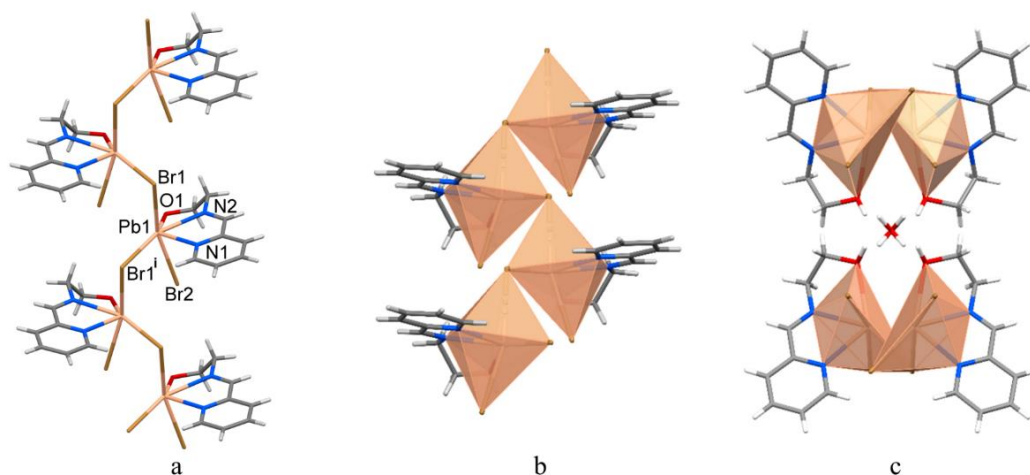


**Figure 3.** (a) Fragment of the double-side organically decorated bromoplumbate(II) chain in **2** [symmetry code:  $i$   $1/2 - x, y, 1/2 + z$ ]; (b) polyhedral representation of the same fragment; (c) fragment of the crystal packing viewed down the  $c$ -axis showing spatial arrangement of two bromoplumbate(II) chains to form a hydrophilic channel filled with water molecules.

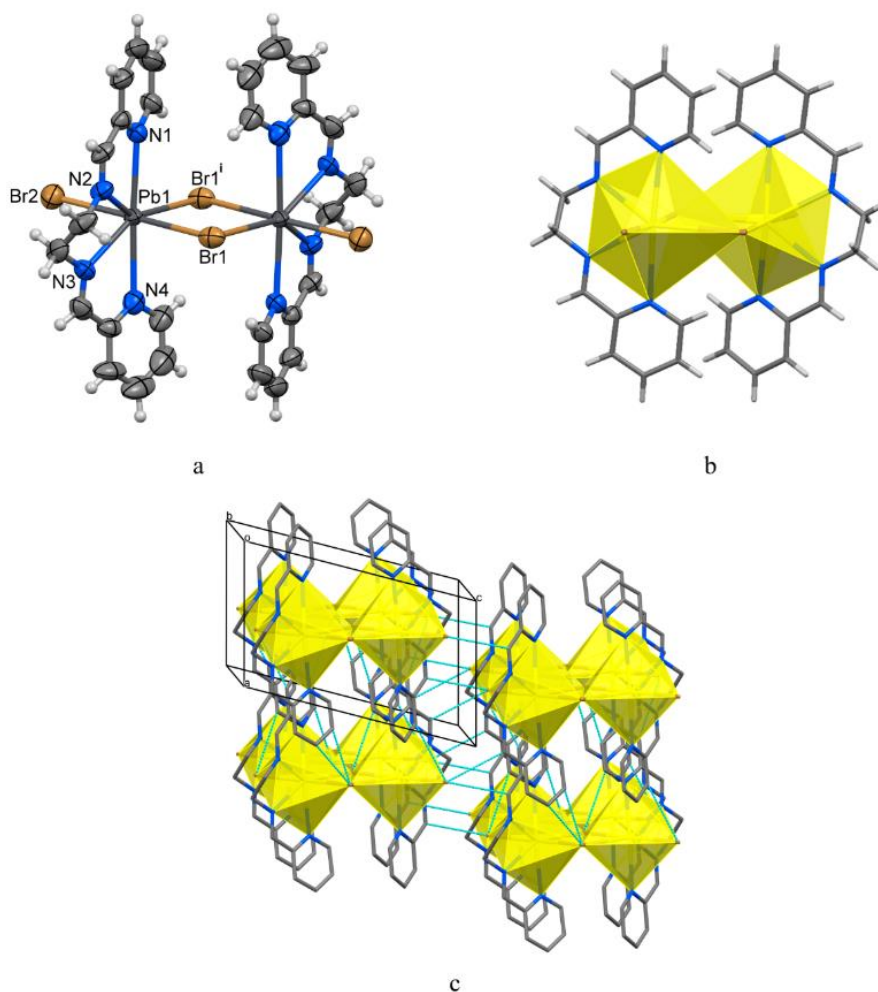


**Figure 4.** (a) Molecular structure and principal atom labelling of  $[\text{PbBr}_2(\text{L}3)]_2$  (**3**), ellipsoids are shown at the 50% probability level [symmetry code:  $i$   $1 - x, 1 - y, 1 - z$ ]; (b) the same molecule in a polyhedral form; (c) fragment of the 3D supramolecular network in **3** stabilized with  $\text{C-H}\cdots\text{Br}$  hydrogen bonds (shown in blue, H atoms omitted).

In the solid state, the dimeric molecules of **3** are stacked identically, forming columns parallel to the *ab* plane, with the  $\text{Pb}_2\text{Br}_4$  moieties in the column being strictly coplanar (Figure 4c). The minimal  $\text{Pb}\cdots\text{Pb}$  distance in the lattice is 8.1348(6) Å; no effective  $\pi$ -overlap is observed.  $\text{C}-\text{H}\cdots\text{Br}$  hydrogen bonding (Table 3) consolidates an extended supramolecular 3D network structure (Figure 4c). The contacts strength depends on their direction in the crystal lattice. In the *ab* plane, the interactions are represented by four distinct crystallographically independent  $\text{C}-\text{H}\cdots\text{Br}$  hydrogen bonds with  $d(\text{C}\cdots\text{Br}) < 3.9$  Å (Table 3). Every dimeric molecule of **3** forms 16 respective contacts with the four nearest molecules in the *ab* plane. The dimeric molecules along the *c* axis are bridged by weaker  $\text{C}-\text{H}\cdots\text{Br}$  hydrogen bonds with  $d(\text{C}\cdots\text{Br}) > 3.9$  Å (Table 3).

### 3.3. Hirshfeld Surface and QTAIM Analyses

The set of intermolecular interactions in complex **1** can be viewed as a combination of contacts between crystallographically independent (N12, N13A) and (N22, N23A)  $[\text{L1}]^+$  cations, negatively charged  $[\text{Pb}_2\text{Cl}_6]_n^{2n-}$  chains and water molecules. The HS of both  $[\text{L1}]^+$  cations surrounding a fragment of the  $[\text{Pb}_2\text{Cl}_6]_n^{2n-}$  chain is shown in Figure 5. Here, and further on, the colours on the surface correspond to shortened contacts (red), van der Waals (vdW) interactions (white) and contacts with longer distances (blue).

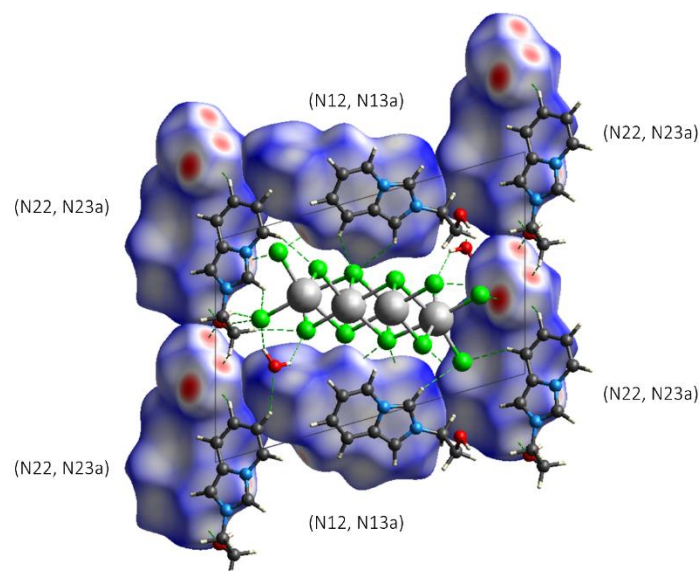


**Figure 5.** Hirshfeld surface mapped over  $d_{\text{norm}}$  of (N12, N13a) and (N22, N23A)  $[\text{L1}]^+$  cations for compound **1** (view along the *a* axis, the major component of the disordered (N22, N23A) cation is shown).

Both  $[\text{L1}]^+$  cations reveal involvement in several distinct hydrogen bonds (Table 3), which are identifiable in the fingerprint plots (Figure 6). The plots are characterized by broad segments of  $\text{H}\cdots\text{H}$  interactions (Figure 6), while the  $\text{C}\cdots\text{C}$  ones are much less abundant (5.4 and 4.3% for (N12, N13A) and (N22, N23A) independent cations, respectively, Figure S4).

The weak interactions between the stacked cations were evaluated by the analysis of reduced density gradient (RDG) [31] of the electron density calculated at the  $\omega\text{B97M-V/ZORA-def2-TZVPP}$  level using crystallographic atomic coordinates (Figure 7). In line with the HS analysis results, the non-covalent contacts in the tetramer  $\{(\text{N12, N13A})\text{-}[\text{L1}]_4\cdot 2\text{H}_2\text{O}\}^{4+}$  are mostly characterized by the broad vdW areas between stacked imidazo[1,5-*a*]pyridine moieties. These findings indicate that  $[\text{L1}]^+$  cations in their stacks are too offset to engage in appreciable  $\pi$ -bonding. At the same time, the chain of (N12, N13A)- $[\text{L1}]^+$  cations is supported by the strong attractive interactions involving water molecules ( $\text{O121}-\text{H121}\cdots\text{O01W}$ ), for which the electron density at the bond critical

point— $\rho_{\text{BCP}}(\mathbf{r})$  (3, -1) between the H121 and O01W atoms—is 0.02504 a.u. According to the dependence for charged assemblies reported in [42], the obtained value of  $\rho_{\text{BCP}}(\mathbf{r})$  corresponds to 39.3 kJ mol<sup>-1</sup> of binding energy (BE) between the (N12, N13A)-[L1]<sup>+</sup> cation and water molecule. However, as the BE vs.  $\rho_{\text{BCP}}(\mathbf{r})$  dependences [42] were developed for assemblies with a single overall charge (in contrast to 4+ charge of the tetramer), the obtained binding energy value has only indicative significance.

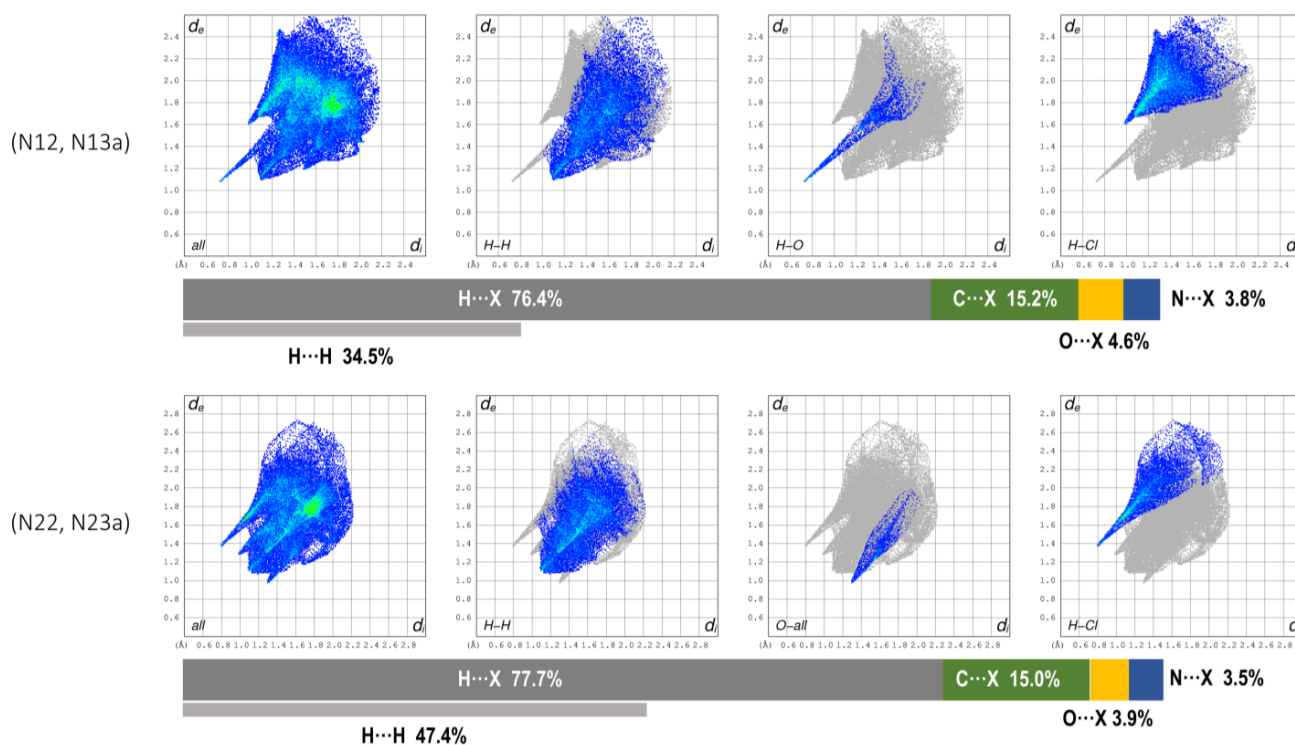


**Figure 6.** Fingerprint plots of (N12, N13A) and (N22, N23A, major component) [L1]<sup>+</sup> cations in the crystal structure of **1** showing the specific  $X_i \cdots X_e$  interactions (where  $X = \text{Cl}, \text{O}$  or  $\text{H}$ ) and their contributions (in %).

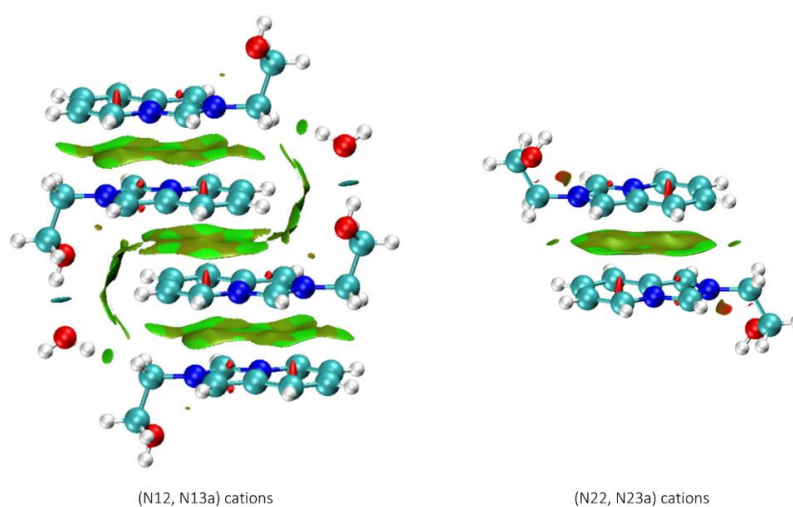


**Figure 7.** Reduced density gradient surfaces (isovalued of 0.5) showing vdW interactions (green area) between [L1]<sup>+</sup> cations and strong hydrogen bonds with participation of water molecules in the crystal structure of **1** (the major component of the disordered (N22, N23A) cation is shown). The colour scheme corresponds to the  $\text{sign}(\lambda_2)\rho(\mathbf{r})$  function with the second largest eigenvalue of the Hessian of electron density,  $\lambda_2$ , at respective points: negative (blue, strong attraction), nearly zero (green, vdW interaction), positive (red, strong repulsion).

The monomeric fragment  $[\text{PbBr}_2(\text{L}2)]$  of the 1D chain in complex **2** was used to construct the Hirshfeld surface (Figure 8). The fingerprint plots disclose several distinct non-covalent contacts mostly  $\text{H}\cdots\text{O}$  and  $\text{H}\cdots\text{Br}$  in nature (Figures 8 and S5). The strongest hydrogen bonds between O1 and O1W atoms are reflected by sharp “peaks” having the shortest  $d_e$  and  $d_i$  distances in the fingerprint plots (Figures 8 and S5). The  $\rho_{\text{BCP}}(\mathbf{r})$  electron density at BCP between H1 and O1W atoms was estimated as 0.01986 a.u., from which the binding energy of the respective contact can be evaluated as  $-15.4 \text{ kJ mol}^{-1}$  (according to the equation for non-charged assemblies [42]). This energy strength can be classified as “weak-to-medium” [42]. The RGD isosurfaces of the vdW contacts between the aromatic groups in **2** are shown in Figure 9.

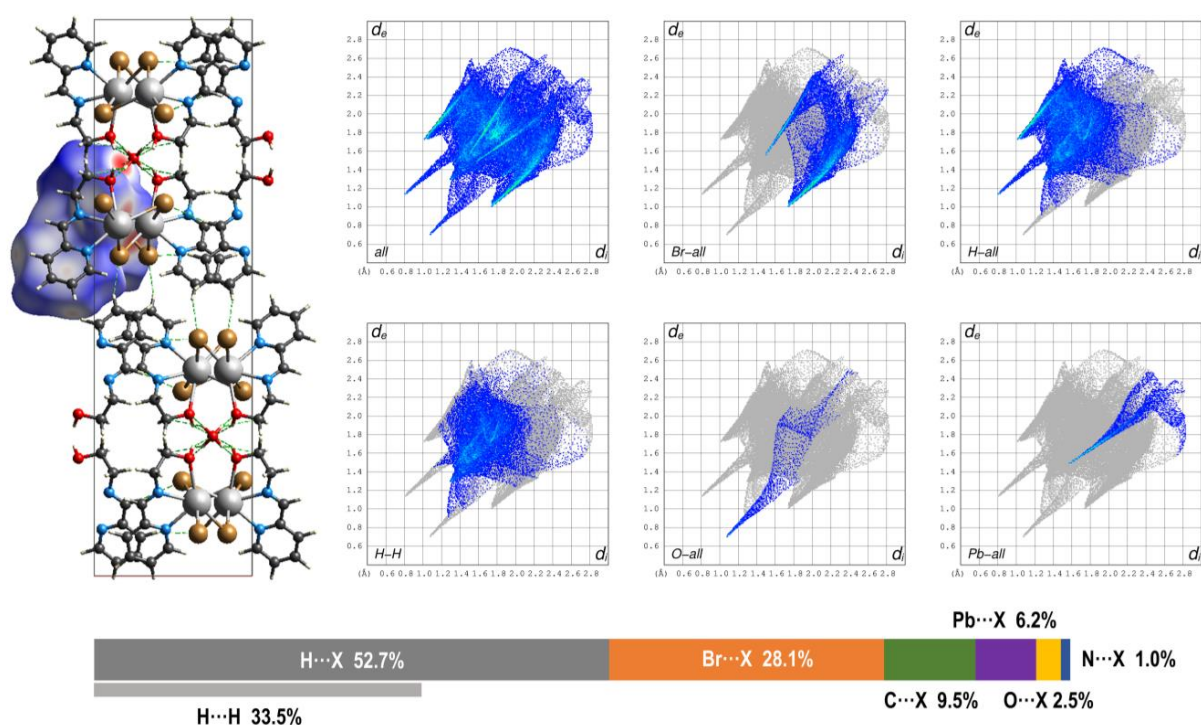


**Figure 8.** Top left: fragment of the crystal structure of **2** viewed down the  $c$  axis showing the HS of the fragment  $[\text{PbBr}_2(\text{L}2)]$ . Top right: selected fingerprint plots. Bottom: contributions of the specific  $X_i\cdots X_e$  contacts.

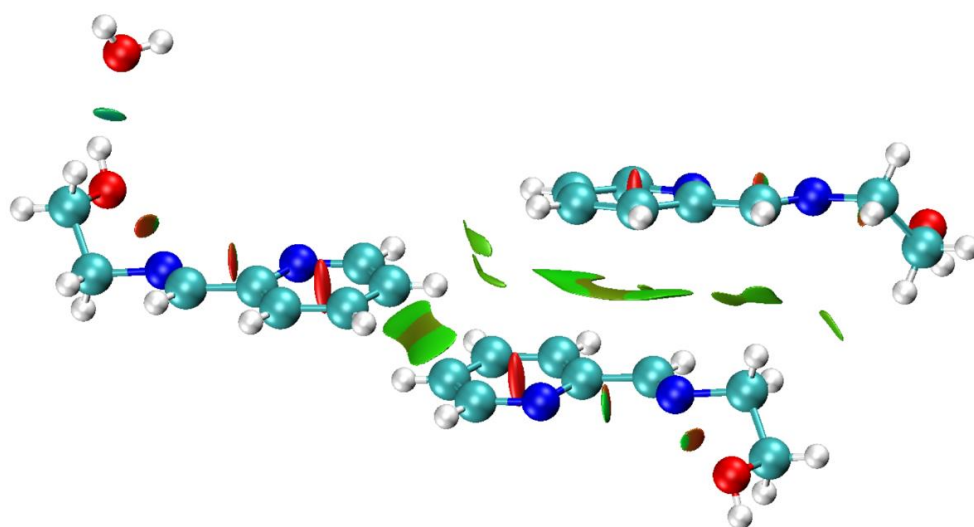


**Figure 9.** Reduced density gradient surfaces (isovalued of 0.5) showing vdW interactions (green area) between aromatic fragments and strong hydrogen bonds involving water molecule for compound **2**.

The dimeric molecules of **3** create a network of non-covalent interactions, of which the highest contribution (40.9%) to the HS is from numerous H···H contacts (Figures 10 and S6). The latter form a broad surface with no distinct directions (Figure 11), except of the C8–H8A···H8A<sup>1</sup>–C8<sup>1</sup> (<sup>1</sup> = 2 – *x*, –*y*, –*z*) interaction between methylene groups [ $d(\text{C}\cdots\text{C}) = 4.379(15) \text{ \AA}$ ] and a pair of weak interactions between pyridine rings C13–H13A···H14A–C14<sup>1</sup> and C14–H14A···H13A–C13<sup>1</sup> [<sup>1</sup> = 2 – *x*, 1 – *y*, 1 – *z*;  $d(\text{C}\cdots\text{C}) = 4.072(18) \text{ \AA}$ ]. As can be seen from the particular Hirshfeld surface, the Br···H and H···Br contacts are mostly located in the *ac* plane (Figure 11). Since the molecules of **3** has no electrical charge, the strengths of these contacts can be estimated [42] from the  $\rho_{\text{BCP}}(\mathbf{r})$  electron density with sufficient precision (Table 4).

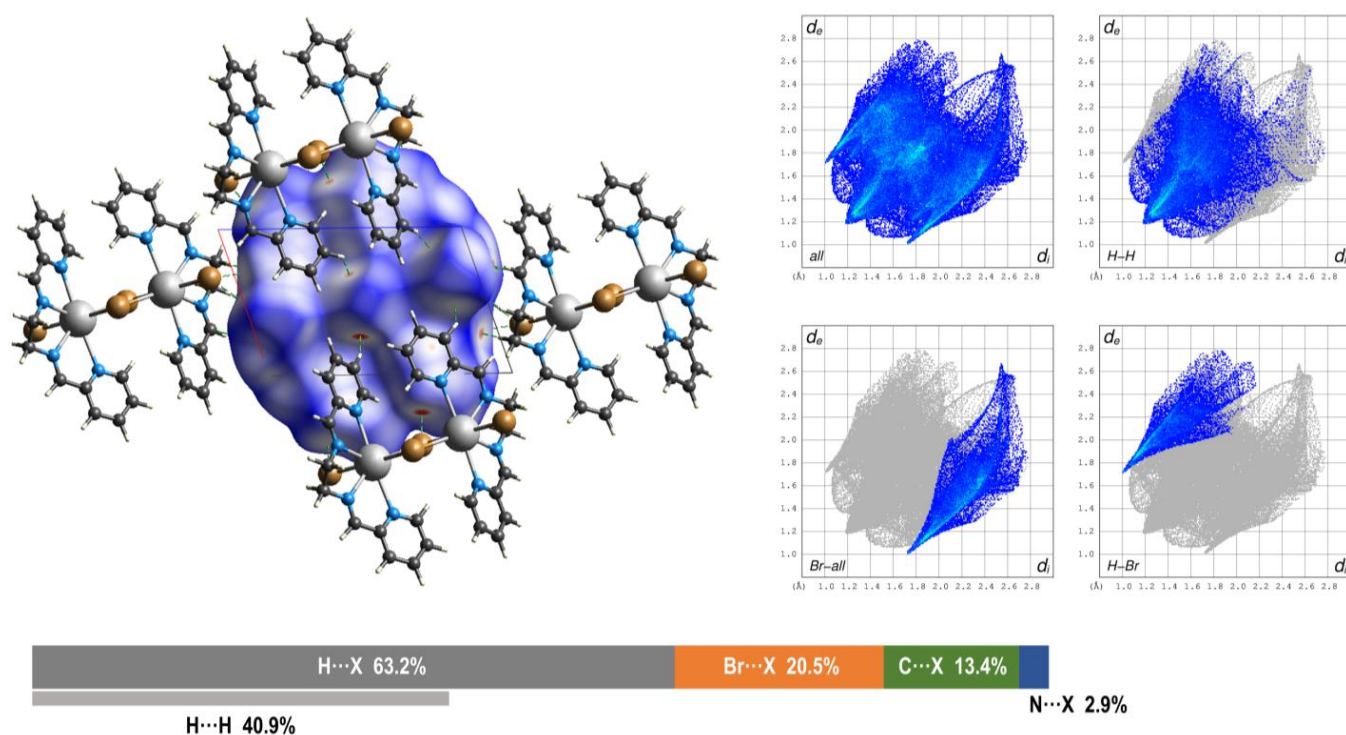


**Figure 10.** Left: Hirshfeld surface of the dinuclear molecule of **3** surrounded by the closest molecules (view along the *b* axis). Right: selected fingerprint plots of the respective surface. Bottom: contributions (in %) of specific  $X_i\cdots X_e$  interactions.

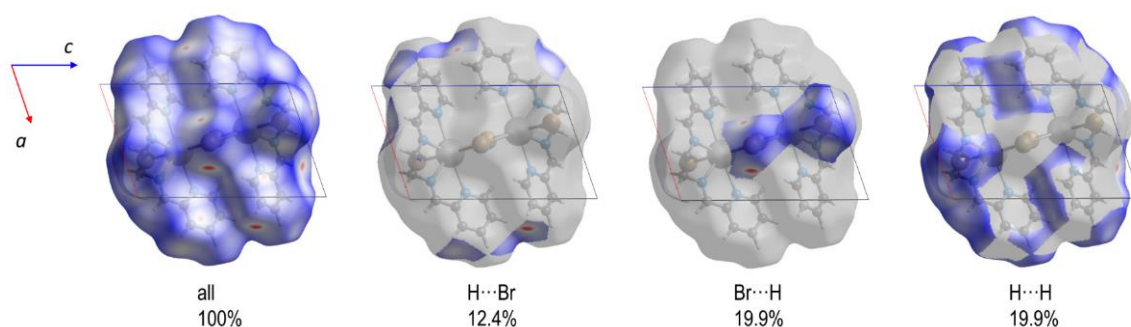


**Figure 11.** Hirshfeld surface of the dinuclear molecule of **3** highlighting regions of specific interactions.

**Table 4.** Electron density at the H...Br BCP and respective binding energies for selected intermolecular contacts in the structure **3** [a].

Contact	$\rho_{\text{BCP}}(\mathbf{r})$ , a.u.	Binding energy, kJ mol <sup>-1</sup>
C2–H2A...Br1 <sup>14</sup> [b]	$8.79 \times 10^{-3}$	-5.10
C4–H4B...Br2 <sup>3</sup>	$6.01 \times 10^{-3}$	-2.50
C6–H6A...Br2 <sup>-5</sup>	$5.32 \times 10^{-3}$	-1.86
C7–H7A...Br2 <sup>-5</sup>	$5.38 \times 10^{-3}$	-1.92
C11–H11A...Br2 <sup>15</sup>	$6.19 \times 10^{-3}$	-2.67
C13–H13A...Br1 <sup>13</sup>	$7.71 \times 10^{-3}$	-4.09

[a] binding energies were estimated according to the equation for non-charged assemblies [42]; [b] symmetry operations have the same numbering as those in Table 3.

Inspection of the geometry and Hirshfeld surface suggests the existence of the contact C8–H8B...C6<sup>1</sup> [<sup>1</sup> = 1 - x, 1 - y, -z;  $d(\text{C}\cdots\text{C}) = 3.722(10)$  Å,  $\angle(\text{C}-\text{H}\cdots\text{C}) = 161.1^\circ$ ] between methylene CH<sub>2</sub> group and imine carbon atom of the neighboring molecules. However, despite the hydrogen atom being clearly oriented towards C6 one, the respective bond critical point is located rather between H8B and C5<sup>1</sup> atoms (Figure 12). Further analysis of the RDG isosurfaces disclosed the existence of a broad non-covalent interaction region between H8B donor and C4<sup>1</sup>, C5<sup>1</sup> and C6<sup>1</sup> (<sup>1</sup> = 1 - x, 1 - y, -z) atoms as acceptors containing 0.0054 electrons (Figure 12). The negative  $q_{\text{bind}}$  index [43] of this domain (-0.00046383) accounts for a weak attractive interaction. The aromatic moieties of the ligand L3 in the molecule of **3** contact each other through vdW interactions (Figure S7).

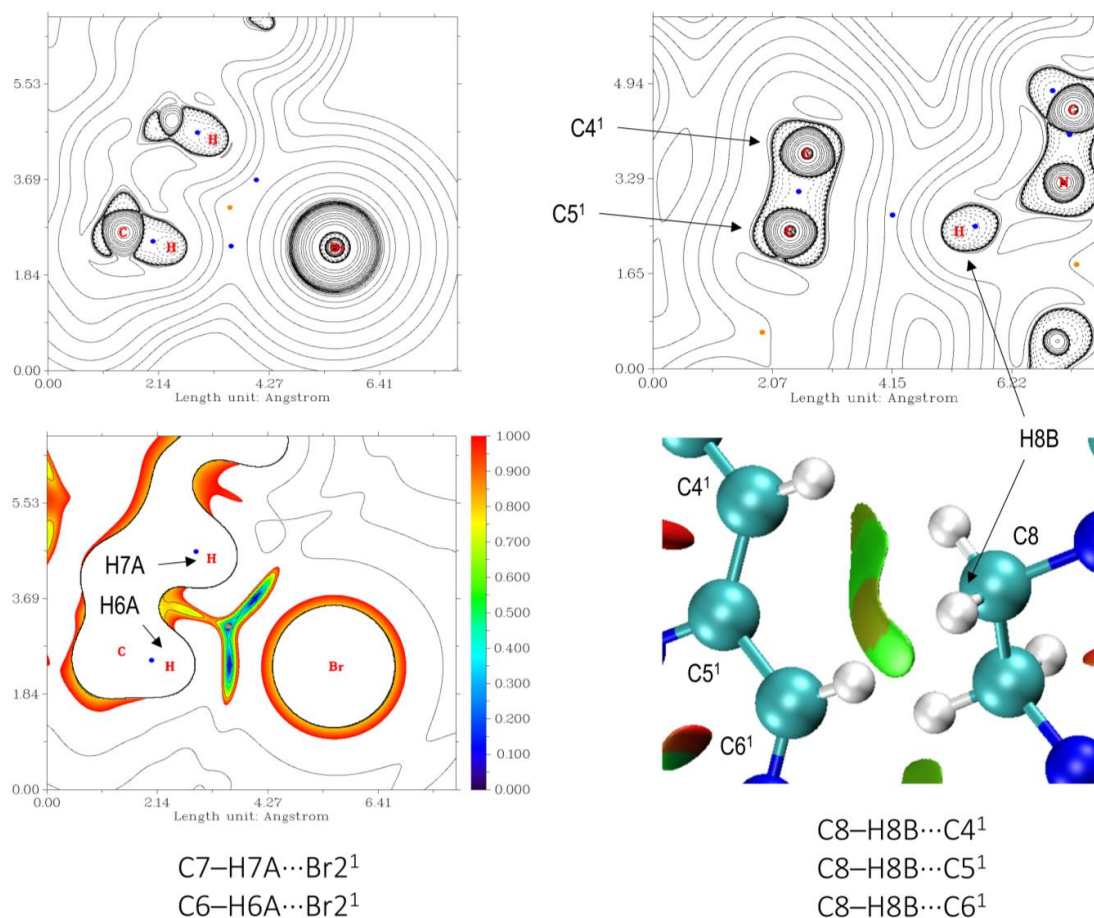


**Figure 12.** Top: plots of the Laplacian of the electron density in the real space,  $\nabla^2\rho(\mathbf{r})$ , for selected weak contacts. Bottom left: 2D cut plane of the RDG function for the same projection as in the top left plot. Bottom right: 3D isosurface of the RDG (isovalue of 0.5) illustrating non-covalent interactions in the H8B–C4<sup>1</sup>/C5<sup>1</sup>/C6<sup>1</sup> groups of atoms (<sup>1</sup> = 1 - x, 1 - y, -z).

### 3.4. Optical Properties of 1–3

The optical diffuse reflectance spectra of all the compounds were measured using powder samples at r.t. (Figure 13a). According to the analysis of the spectra by the Tauc plot based on the assumption of direct band gap,  $[F(R)h\nu]^2$  vs.  $h\nu$  (where  $F(R)$  denotes the Kubelka–Munk function,  $h\nu$  is photon energy in eV), the optical band gap values of 1, 2 and 3 were estimated to be 3.36, 3.13 and 2.96 eV, respectively (Figure 13b). The values of 1 and 2 are comparable to those of reported 1D hybrid lead perovskites, such as  $[\text{H}_2\text{bpp}]\text{Pb}_2\text{Cl}_6$  (3.55 eV),  $[\text{H}_2\text{bpp}]\text{Pb}_2\text{Br}_6$  (3.30 eV; bpp = 1,3-bis(4-pyridyl)-propane) [38],  $[\text{2,6-dmpz}]_3\text{Pb}_2\text{Br}_{10}$  (3.12 eV; 2,6-dmpz = 2,6-dimethylpiperazine),  $[\text{hex}]\text{PbBr}_3$  (3.41 eV; hex = hexamethyleneimine),  $[\text{hep}]\text{PbBr}_3$  (3.50 eV; hep = heptamethyleneimine) [39]. Using density functional theory calculations,  $[\text{2,6-dmpz}]_3\text{Pb}_2\text{Br}_{10}$ ,  $[\text{hex}]\text{PbBr}_3$  and  $[\text{hep}]\text{PbBr}_3$  were found to be direct band gap semiconductors [39]. Their valence band maximum (VBM) is composed of mixed Br-p and Pb-s orbitals, while empty Pb-p orbitals constitute conduction band minimum (CBM). In the case of two  $\text{H}_2\text{bpp}$  hybrid lead halides, the VBM was derived from hybridization of Pb-6p and Cl-3p or Br-4p orbitals, and CBM mainly originated from the C-2p/N-2p states of the bicyclic organic cations [38].

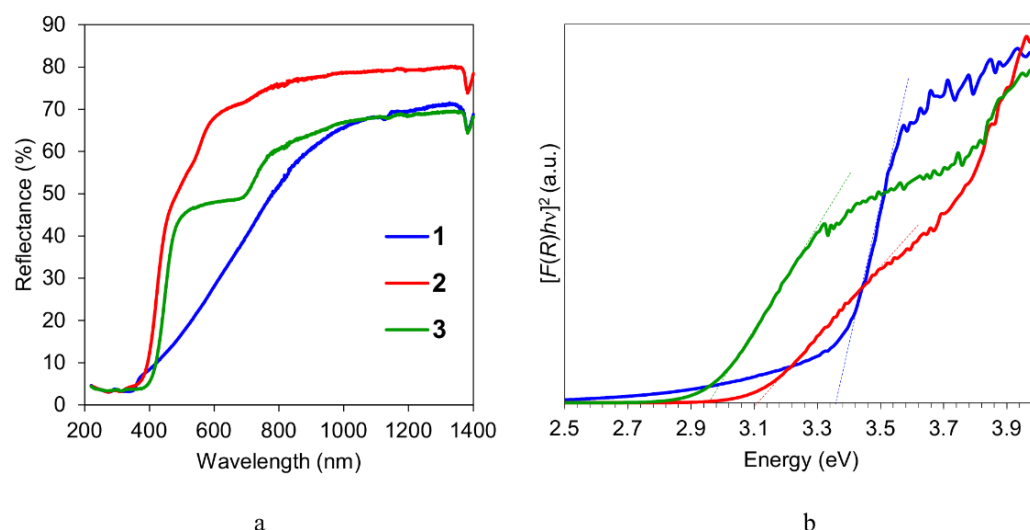


**Figure 13.** Diffuse reflectance spectra measured using powder samples of 1–3 at r.t. (a) and the Tauc plots in the range 2.5–4 eV based on the assumption of direct band gap calculated from the reflectance spectra of 1–3 (b).

Within the series of 1D and 2D lead bromide hybrids [39], the electronic structure was suggested to depend on the connectivity mode of  $\text{PbBr}_6$  octahedra, where the corner-connected compound  $[\text{4-amp}]\text{PbBr}_4$  [4-amp-4-(aminomethyl)piperidine] exhibits the smallest band gap value (2.93 eV). The face-sharing compounds  $[\text{hex}]\text{PbBr}_3$  and  $[\text{hep}]\text{PbBr}_3$  possess larger band gaps than  $[\text{2,6-dmpz}]_3\text{Pb}_2\text{Br}_{10}$  with the edge- and corner-connecting structure. The band gaps successively going up from “corner-sharing” to “edge-sharing” and further “face-sharing” have also been observed in the lead iodide perovskite-derived organic–inorganic hybrids [44]. The band gaps of edge-sharing 1 and corner-sharing 2 perovskites follow the general trend.

## 4. Conclusions

In this study, we aimed to explore the templating effect of imidazo[1,5-*a*]pyridinium-based cation with hydroxyl functionality on the dimensionality of the lead halide anionic framework and connectivity modes of the  $[\text{PbHal}_6]^{4-}$  octahedra, as well as H-bonding interactions in the resulting hybrid lead halide perovskite. To this aim, Ea·HCl was used in the developed protocol for the synthesis of substituted imidazo[1,5-*a*]pyridinium cations by the acid catalyzed oxidative cyclocondensation of FA, amine and 2-PCA. The obtained in situ  $[\text{L1}]^+$  cation directed the formation of the 1D chloroplumbate  $[\text{L1}]_{2n}[\text{Pb}_2\text{Cl}_6]_{n\infty} \cdot n\text{H}_2\text{O}$

(1), revealing a new type of the  $[\text{Pb}_2\text{Cl}_6]_\infty$  twin chain constructed from three-edge- and five-edge-sharing  $\text{PbCl}_6$  octahedra. In the case of  $[\text{PbBr}_2(\text{L}2)]_{\text{n}\infty} \cdot 0.5\text{nH}_2\text{O}$  (2) and  $[\text{PbBr}_2(\text{L}3)]_2$  (3), the introduction of HBr—the necessary acid component and source of bromide anions—directly to the reaction media subverted the expected oxidation cyclization and instead facilitated the amine-aldehyde condensation between 2-PCA and Ea or En, respectively. The isolated hybrid lead bromide 2 features a chain of corner-sharing  $\text{PbBr}_3\text{N}_2\text{O}$  octahedra, decorated with the tridentate Schiff base ligands on both sides. In the 0D dimer 3, two irregular  $\text{PbBr}_3\text{N}_4$  pentagonal bipyramids are connected by edge sharing. The Hirshfeld surface and QTAIM analyses disclosed the presence of numerous weak interactions between molecular and polymeric fragments in the structures of 1–3. The band gaps of 1 (3.36 eV) and 2 (3.13 eV) with different connectivity follow the general trend of edge-sharing perovskites exhibiting larger band gaps than corner-sharing structures.

**Supplementary Materials:** The following supporting information can be downloaded at: <https://www.mdpi.com/article/10.3390/cryst13020307/s1>, Figure S1: IR spectrum of  $[\text{L}1]_{2\text{n}}[\text{Pb}_2\text{Cl}_6]_{\text{n}\infty} \cdot \text{nH}_2\text{O}$  (1); Figure S2: IR spectrum of  $[\text{PbBr}_2(\text{L}2)]_{\text{n}\infty} \cdot 0.5\text{nH}_2\text{O}$  (2); Figure S3: IR spectrum of  $[\text{PbBr}_2(\text{L}3)]_2$  (3); Figure S4: Selected fingerprint plots of the (N12, N13A) and (N22, N23A, major component)  $[\text{L}1]^+$  cations in the crystal structure of 1 showing  $X_i \cdots X_e$  interactions (where  $X = \text{Cl}, \text{O}, \text{C}$  or  $\text{H}$ ); Figure S5: Selected fingerprint plots of the fragment  $[\text{PbBr}_2(\text{L}2)]$  in the crystal structure of 2 showing  $X_i \cdots X_e$  interactions (where  $X = \text{Br}, \text{O}, \text{C}$  or  $\text{H}$ ); Figure S6: Selected fingerprint plots of the dinuclear molecule of 3 showing  $X_i \cdots X_e$  interactions (where  $X = \text{Br}, \text{N}, \text{C}$  or  $\text{H}$ ); Figure S7: Reduced density gradient surfaces (isovalue of 0.5) showing weak vdW interactions (green area) between aromatic fragments of the ligands L3 in the molecular structure of 3 (lead and bromine atoms were excluded from calculations).

**Author Contributions:** Conceptualization, O.Y.V.; methodology, O.Y.V. and D.S.N.; investigation, O.Y.V., E.A.B., O.V.N. A.N.S. and D.S.N.; writing—original draft preparation, O.Y.V. and D.S.N.; writing—review and editing, O.Y.V. All authors have read and agreed to the published version of the manuscript.

**Funding:** The work was performed with the support of the Ministry of Education and Science of Ukraine (project 22BP037-13, grant for the perspective development of the scientific direction ‘Mathematical sciences and natural sciences’ at the Taras Shevchenko National University of Kyiv) and the Fundação para a Ciência e Tecnologia (FCT), Portugal (projects UIDB/00100/2020, UIDP/00100/2020, and LA/P/0056/2020 of Centro de Química Estrutural, contracts IST-ID/086/2018 and IST-ID/117/2018).

**Data Availability Statement:** Crystallographic data for the structures reported can be obtained free of charge from the Cambridge Crystallographic Data Centre via [www.ccdc.cam.ac.uk/data-request/cif](http://www.ccdc.cam.ac.uk/data-request/cif) (accessed on 27 January 2023) quoting the deposition numbers CCDC 2217143 (1), 2223148 (2) and 2223147 (3).

**Conflicts of Interest:** The authors declare no conflict of interest.

## References

1. Green, M.A.; Hishikawa, Y.; Warta, W.; Dunlop, E.D.; Levi, D.H.; Hohl-Ebinger, J.; Ho-Baillie, A.W. Solar cell efficiency tables (version 50). *Prog. Photovolt. Res. Appl.* **2017**, *25*, 668–676. [[CrossRef](#)]
2. Sutherland, B.R.; Sargent, E.H. Perovskite photonic sources. *Nat. Photon.* **2016**, *10*, 295–302. [[CrossRef](#)]
3. Saparov, B.; Mitzi, D.B. Organic-Inorganic Perovskites: Structural Versatility for Functional Materials Design. *Chem. Rev.* **2016**, *116*, 4558–4596. [[CrossRef](#)] [[PubMed](#)]
4. Smith, M.D.; Jaffe, A.; Dohner, E.R.; Lindenberg, A.M.; Karunadasa, H.I. Structural origins of broadband emission from layered Pb–Br hybrid perovskites. *Chem. Sci.* **2017**, *8*, 4497–4504. [[CrossRef](#)]
5. Yuan, Z.; Zhou, C.; Tian, Y.; Shu, Y.; Messier, J.; Wang, J.C.; Van De Burgt, L.J.; Kountouriotis, K.; Xin, Y.; Holt, E.; et al. One-dimensional organic lead halide perovskites with efficient bluish white-light emission. *Nat. Commun.* **2017**, *8*, 14051. [[CrossRef](#)]
6. Peng, Y.; Yao, Y.; Li, L.; Wu, Z.; Wang, S.; Luo, J. White-light emission in a chiral one-dimensional organic–inorganic hybrid perovskite. *J. Mater. Chem. C* **2018**, *6*, 6033–6037. [[CrossRef](#)]
7. Buvaylo, E.A.; Kokozay, V.N.; Linnik, R.P.; Vassilyeva, O.Y.; Skelton, B.W. Hybrid organic–inorganic chlorozincate and a molecular zinc complex involving the in situ formed imidazo [1,5-*a*]pyridinium cation: Serendipitous oxidative cyclization, structures and photophysical properties. *Dalton Trans.* **2015**, *44*, 13735–13744. [[CrossRef](#)]

8. Vassilyeva, O.Y.; Buvaylo, E.A.; Linnik, R.P.; Nesterov, D.S.; Trachevsky, V.V.; Skelton, B.W. Synthetic strategy towards halometalates with imidazo [1,5-*a*]pyridinium-based counterions. *CrystEngComm* **2020**, *22*, 5096–5105. [[CrossRef](#)]
9. Vassilyeva, O.Y.; Buvaylo, E.A.; Kokozay, V.N.; Skelton, B.W.; Sobolev, A.N. Crystal structures of an imidazo[1,5-*a*] pyridinium-based ligand and its (C<sub>13</sub>H<sub>12</sub>N<sub>3</sub>)<sub>2</sub>[CdI<sub>4</sub>] hybrid salt. *Acta Cryst.* **2019**, *75*, 1209–1214. [[CrossRef](#)]
10. Vassilyeva, O.; Buvaylo, E.; Kokozay, V.; Skelton, B.W.; Rajnák, C.; Titis, J.; Boca, R. Long magnetic relaxation time of tetracoordinate Co<sup>2+</sup> in imidazo [1,5-*a*]pyridinium-based (C<sub>13</sub>H<sub>12</sub>N<sub>3</sub>)<sub>2</sub>[CoCl<sub>4</sub>] hybrid salt and [Co(C<sub>13</sub>H<sub>12</sub>N<sub>3</sub>)Cl<sub>3</sub>] molecular complex. *Dalton Trans.* **2019**, *48*, 11278–11284. [[CrossRef](#)] [[PubMed](#)]
11. Vassilyeva, O.Y.; Buvaylo, E.A.; Lobko, Y.V.; Linnik, R.P.; Kokozay, V.N.; Skelton, B.W. Organic–inorganic hybrid tetrachlorocadmates as promising fluorescent agents for cross-linked polyurethanes: Synthesis, crystal structures and extended performance analysis. *RSC Adv.* **2021**, *11*, 7713–7722. [[CrossRef](#)] [[PubMed](#)]
12. Vassilyeva, O.Y.; Buvaylo, E.A.; Kokozay, V.N.; Skelton, B.W. Organic-inorganic hybrid mixed-halide Zn<sup>II</sup> and Cd<sup>II</sup> tetrahalometalates with the 2-methylimidazo[1,5-*a*]pyridinium cation. *Acta Cryst.* **2022**, *78*, 359–364. [[CrossRef](#)] [[PubMed](#)]
13. Lyons, A.S.; Ingersoll, M.A.; Muniyan, S.; D’Cunha, N.; Robinson, T.; Hoelting, K.; Dwyer, J.G.; Biu, X.R.; Batra, S.K.; Lin, M.F. Novel imidazopyridine derivatives possess anti-tumor effect on human castration-resistant prostate cancer cells. *PLoS ONE* **2015**, *10*, e0131811.
14. Song, G.J.; Bai, S.Y.; Dai, X.; Cao, X.Q.; Zhao, B.X. A ratiometric lysosomal pH probe based on the imidazo[1,5-*a*]pyridine–rhodamine FRET and ICT system. *RSC Adv.* **2016**, *6*, 41317–41322. [[CrossRef](#)]
15. Volpi, G.; Garino, C.; Fresta, E.; Casamassa, E.; Giordano, M.; Barolo, C.; Viscardi, G. Strategies to increase the quantum yield: Luminescent methoxylated imidazo[1,5-*a*]pyridines. *Dyes Pigment.* **2021**, *192*, 109455. [[CrossRef](#)]
16. Yagishita, F.; Nii, C.; Tezuka, Y.; Tabata, A.; Nagamune, H.; Uemura, N.; Yoshida, Y.; Mino, T.; Sakamoto, M.; Kawamura, Y. Fluorescent N-heteroarenes having large Stokes shift and water solubility suitable for bioimaging. *Asian J. Org. Chem.* **2018**, *7*, 1614–1619. [[CrossRef](#)]
17. Kortüm, G.; Braun, W.; Herzog, G. Principles and techniques of diffuse-reflectance spectroscopy. *Angew. Chem. Int. Ed.* **1963**, *2*, 333–341. [[CrossRef](#)]
18. Landi, S., Jr.; Segundo, I.R.; Freitas, E.; Vasilevskiy, M.; Carneiro, J.; Tavares, C.J. Use and misuse of the Kubelka-Munk function to obtain the band gap energy from diffuse reflectance measurements. *Solid State Commun.* **2022**, *341*, 114573. [[CrossRef](#)]
19. Spackman, P.R.; Turner, M.J.; McKinnon, J.J.; Wolff, S.K.; Grimwood, D.J.; Jayatilaka, D.; Spackman, M.A. CrystalExplorer: A program for Hirshfeld surface analysis, visualization and quantitative analysis of molecular crystals. *J. Appl. Cryst.* **2021**, *54*, 1006–1011. [[CrossRef](#)]
20. Sheldrick, G.M. Crystal structure refinement with SHELXL. *Acta Cryst.* **2015**, *71*, 3–8.
21. Neese, F. Software update: The ORCA program system—Version 5.0. *Wil. Interdiscip. Rev. Comput. Mol. Sci.* **2022**, *12*, e1606. [[CrossRef](#)]
22. Neese, F. The ORCA program system. *Wil. Interdiscip. Rev. Comput. Mol. Sci.* **2012**, *2*, 73–78. [[CrossRef](#)]
23. Mardirossian, N.; Head-Gordon, M. ωB97M-V: A combinatorially optimized, range-separated hybrid, meta-GGA density functional with VV10 nonlocal correlation. *J. Chem. Phys.* **2016**, *144*, 214110. [[CrossRef](#)] [[PubMed](#)]
24. Weigend, F.; Ahlrichs, R. Balanced basis sets of split valence, triple zeta valence and quadruple zeta valence quality for H to Rn: Design and assessment of accuracy. *Phys. Chem. Chem. Phys.* **2005**, *7*, 3297–3305. [[CrossRef](#)]
25. Pantazis, D.A.; Neese, F. All-electron scalar relativistic basis sets for the 6p elements. *Theor. Chem. Acc.* **2012**, *131*, 1292. [[CrossRef](#)]
26. Weigend, F. Accurate Coulomb-fitting basis sets for H to Rn. *Phys. Chem. Chem. Phys.* **2006**, *8*, 1057–1065. [[CrossRef](#)] [[PubMed](#)]
27. Stoychev, G.L.; Auer, A.A.; Neese, F. Automatic Generation of Auxiliary Basis Sets. *J. Chem. Theor. Comput.* **2017**, *13*, 554–562. [[CrossRef](#)]
28. van Wüllen, C. Molecular density functional calculations in the regular relativistic approximation: Method, application to coinage metal diatomics, hydrides, fluorides and chlorides, and comparison with first-order relativistic calculations. *J. Chem. Phys.* **1998**, *109*, 392. [[CrossRef](#)]
29. Barone, V.; Cossi, M. Quantum calculation of molecular energies and energy gradients in solution by a conductor solvent model. *J. Phys. Chem. A* **1998**, *102*, 1995–2001. [[CrossRef](#)]
30. Lu, T.; Chen, F.W. Multiwfn: A multifunctional wavefunction analyzer. *J. Comput. Chem.* **2012**, *33*, 580–592. [[CrossRef](#)]
31. Johnson, E.R.; Keinan, S.; Mori-Sanchez, P.; Contreras-Garcia, J.; Cohen, A.J.; Yang, W.T. Revealing Noncovalent Interactions. *J. Am. Chem. Soc.* **2010**, *132*, 6498–6506. [[CrossRef](#)] [[PubMed](#)]
32. Humphrey, W.; Dalke, A.; Schulten, K. VMD—Visual Molecular Dynamics. *J. Mol. Graph.* **1996**, *14*, 33–38. [[CrossRef](#)] [[PubMed](#)]
33. Dobrzycki, L.; Wozniak, K. Inorganic–organic hybrid salts of diaminobenzenes and related cations. *CrystEngComm* **2008**, *10*, 577–589. [[CrossRef](#)]
34. Barkaoui, H.; Abid, H.; Yangui, A.; Triki, S.; Boukheddaden, K.; Abid, Y. Yellowish white-light emission involving resonant energy transfer in a new one-dimensional hybrid material: (C<sub>9</sub>H<sub>10</sub>N<sub>2</sub>)PbCl<sub>4</sub>. *J. Phys. Chem. C* **2018**, *122*, 24253–24261. [[CrossRef](#)]
35. Groom, C.R.; Bruno, I.J.; Lightfoot, M.P.; Ward, S.C. The Cambridge Structural Database. *Acta Cryst.* **2016**, *72*, 171–179. [[CrossRef](#)]
36. Wu, G.; Zhou, C.; Ming, W.; Han, D.; Chen, S.; Yang, D.; Besara, T.; Neu, J.; Siegrist, T.; Du, M.H.; et al. A one-dimensional organic lead chloride hybrid with excitation-dependent broadband emissions. *ACS Energy Lett.* **2018**, *3*, 1443–1449. [[CrossRef](#)]
37. Martinez, C.R.; Iverson, B.L. Rethinking the term “pi-stacking”. *Chem. Sci.* **2012**, *3*, 2191–2201. [[CrossRef](#)]

38. Sun, X.Y.; Yue, M.; Jiang, Y.X.; Zhao, C.H.; Liao, Y.Y.; Lei, X.W.; Yue, C.Y. Combining dual-light emissions to achieve efficient broadband yellowish-green luminescence in one-dimensional hybrid lead halides. *Inorg. Chem.* **2021**, *60*, 1491–1498. [[CrossRef](#)]
39. Mao, L.; Guo, P.; Kepenekian, M.; Hadar, I.; Katan, C.; Even, J.; Schaller, R.D.; Stoumpos, C.C.; Kanatzidis, M.G. Structural diversity in white-light-emitting hybrid lead bromide perovskites. *JACS* **2018**, *140*, 13078–13088. [[CrossRef](#)]
40. Roy, S.; Choubey, S.; Bhar, K.; Khan, S.; Mitra, P.; Ghosh, B.K. Syntheses, structures, and luminescence behavior of terephthalate bridged lead(II) complexes with tetradentate N-donor Schiff bases. *J. Mol. Struct.* **2013**, *1051*, 328–335. [[CrossRef](#)]
41. Hashemi, L.; Morsali, A. Sonochemical synthesis of nano-structured lead(II) complex: Precursor for the preparation of PbO nano-structures. *J. Coord. Chem.* **2011**, *64*, 4088–4097. [[CrossRef](#)]
42. Emamian, S.; Lu, T.; Kruse, H.; Emamian, H. Exploring Nature and Predicting Strength of Hydrogen Bonds: A Correlation Analysis between Atoms-in-Molecules Descriptors, Binding Energies, and Energy Components of Symmetry-Adapted Perturbation Theory. *J. Comput. Chem.* **2019**, *40*, 2868–2881. [[CrossRef](#)] [[PubMed](#)]
43. Contreras-García, J.; Yang, W.; Johnson, E.R. Analysis of Hydrogen-Bond Interaction Potentials from the Electron Density: Integration of Noncovalent Interaction Regions. *J. Phys. Chem. A* **2011**, *115*, 12983–12990. [[CrossRef](#)] [[PubMed](#)]
44. Kamminga, M.E.; de Wijs, G.A.; Havenith, R.W.; Blake, G.R.; Palstra, T.T. The role of connectivity on electronic properties of lead iodide perovskite-derived compounds. *Inorg. Chem.* **2017**, *56*, 8408–8414. [[CrossRef](#)] [[PubMed](#)]

**Disclaimer/Publisher’s Note:** The statements, opinions and data contained in all publications are solely those of the individual author(s) and contributor(s) and not of MDPI and/or the editor(s). MDPI and/or the editor(s) disclaim responsibility for any injury to people or property resulting from any ideas, methods, instructions or products referred to in the content.